NANO LETTERS

pubs.acs.org/NanoLett Letter

Correlation between Electronic Configuration and Magnetic Stability in Dysprosium Single Atom Magnets

Fabio Donati,* Marina Pivetta, Christoph Wolf, Aparajita Singha, Christian Wäckerlin, Romana Baltic, Edgar Fernandes, Jean-Guillaume de Groot, Safa Lamia Ahmed, Luca Persichetti, Corneliu Nistor, Jan Dreiser, Alessandro Barla, Pietro Gambardella, Harald Brune, and Stefano Rusponi*

Cite This: *Nano Lett.* 2021, 21, 8266–8273 Read Online

ACCESS | Metrics & More | Article Recommendations | Supporting Information

ABSTRACT: Single atom magnets offer the possibility of magnetic information storage in the most fundamental unit of matter. Identifying the parameters that control the stability of their magnetic states is crucial to design novel quantum magnets with tailored properties. Here, we use X-ray absorption spectroscopy to show that the electronic configuration of dysprosium atoms on MgO(100) thin films can be tuned by the proximity of the metal Ag(100) substrate onto which the MgO films are grown. Increasing the MgO thickness from 2.5 to 9 monolayers induces a change in the dysprosium electronic configuration from $4f^9$ to $4f^{10}$. Hysteresis loops indicate long magnetic lifetimes for both configurations, however, with a different field-dependent magnetic stability. Combining these measurements with scanning tunneling microscopy, density functional theory, and multiplet calculations unveils the role of the adsorption site and charge transfer to the substrate in determining the stability of quantum states in dysprosium single atom magnets.

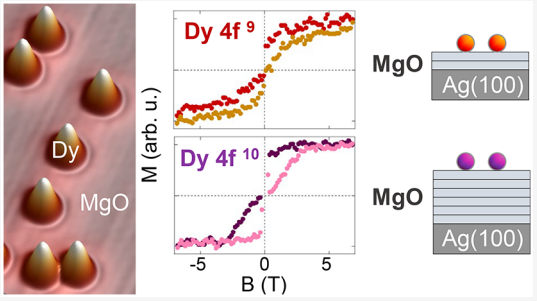

KEYWORDS: *Single atom magnets, lanthanides, X-ray magnetic circular dichroism, scanning tunneling microscopy, density functional theory, multiplet calculations*

Lanthanide-based quantum magnets are model systems for atomic scale memory[1−8] and quantum logic devices.[9,10] Because of their strong localization, their 4f electrons generally show a very limited degree of covalency and preserve an atomic-like character with well-defined integer orbital occupation. Depending on the ligand environment, lanthanide complexes and surface-adsorbed atoms can be mostly found in either atomlike ($4f^n$)[4,11−15] or bulklike configuration ($4f^{n-1}$).[1−3,16−23] Not only does the 4f occupation determine the magnetic moment and stability of the atom, but it also has an impact on the population of the 6s5d valence orbitals[15,22,24,25] determining the behavior in spin transport measurements.[8,26−28] Hence, understanding how to control the lanthanide atom's electronic configuration is a crucial step to develop novel approaches to design quantum magnets with tailored stability and accessibility of their magnetic states.[22,29]

Atom adsorption on suitable surfaces is a viable pathway for creating such quantum magnets[3,4,8] and allowing individual access to their spin states using transport techniques.[8,26−28,30] However, despite the relatively simple atom-support coordination structure, it remains challenging to theoretically predict how the substrate and adsorption geometry impact their multiorbital spin configuration, calling for experiments to shed light on these mechanisms.

Among the lanthanide series, dysprosium (Dy) has been employed to realize molecular magnets with record-high blocking temperature[1,2,19] and surface-supported single atom magnets with long spin lifetime.[4,8] Moreover, recent theoretical calculations on DyO complexes predict large magnetic anisotropy for Dy in both $4f^9$ and $4f^{10}$ electronic configurations.[31,32] Here, we focus on O-coordinated Dy atoms resulting from low-temperature adsorption on MgO thin films grown on Ag(100). We show that the electronic configuration and, consequently, the magnetic properties of the Dy atoms depend on the thickness of the supporting MgO layer. For MgO layers with an average thickness t_{MgO} < 5 monolayers (ML), X-ray absorption spectroscopy (XAS) and magnetic circular dichroism (XMCD) at 2.5 K reveal a predominance of bulklike Dy $4f^9$ configuration, displaying magnetic hysteresis indicative of long lifetimes. By increasing the thickness of the MgO layer, Dy atoms with $4f^{10}$ configuration progressively increase in abundance and become the dominant species for t_{MgO} > 6−7 ML. Remarkably, Dy atoms show magnetic hysteresis also in this configuration, however, with a character-

Received: July 15, 2021
Revised: September 20, 2021
Published: September 27, 2021

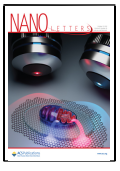

https://doi.org/10.1021/acs.nanolett.1c02744
Nano Lett. 2021, 21, 8266–8273

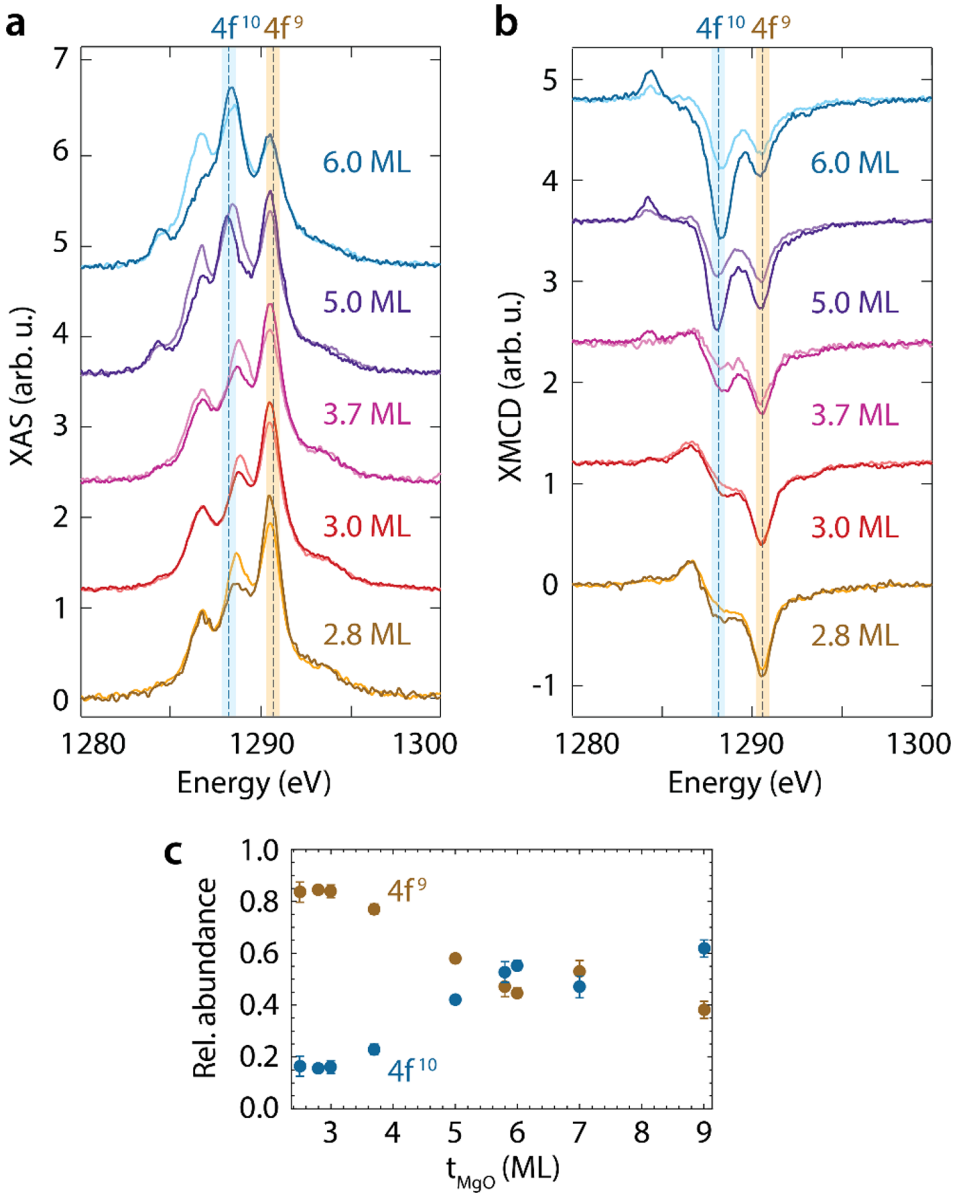

Figure 1. 4f occupation versus MgO thickness for Dy atoms on MgO/Ag(100). (a) XAS and (b) XMCD at the Dy M_5 edge as a function of the average MgO thickness t_{MgO}. Fractional values of t_{MgO} indicate incomplete filling of the MgO atomic layers. Darker/lighter lines show the measurement at normal/grazing incidence, respectively. The position of the $4f^9$ and $4f^{10}$ main peaks of XAS and XMCD measurements are indicated with light blue and brown bands, respectively. (Dy coverage Θ_{Dy} = 0.004−0.014 ML, B = 6.8 T, T = 2.5 K). (c) Relative abundance of the $4f^9$ and $4f^{10}$ species obtained by fitting the experimental data with simulated spectra from multiplet calculations (see SI for details). Standard deviations from the fit are displayed as error bars.

istic butterfly loop indicating quantum tunneling of the magnetization (QTM) in the absence of an external field. Magnetic relaxation measurements reveal that the lifetime of magnetic states can be controlled using the external field, with a maximum of about 200 s for 0.25−0.40 T. Density functional theory (DFT) and multiplet calculations reveal how charge transfer to the substrate and adsorption geometry determine the electronic configuration of Dy and the stability of its magnetic states.

We perform XAS/XMCD measurements at the $M_{4,5}$ edges (3d → 4f transitions) of Dy at 6.8 T and 2.5 K at the EPFL/PSI X-Treme beamline at the Swiss Light Source[33] to determine the 4f orbital occupation and magnetic properties. To avoid measurements on exposed Ag(100) regions, we use MgO films with t_{MgO} > 2 ML. XAS/XMCD spectra are acquired in two different geometries, that is, with the photon beam and magnetic field oriented along the surface normal (normal incidence) and 60° off-normal (grazing incidence, see SI for details), to determine the magnetization easy axis of the Dy atoms.[4,11,12,34]

The XAS and XMCD spectra as a function of the average MgO thickness are displayed in Figure 1a,b, respectively. The energy of the maximum at the M_5 edge, both in XAS and XMCD, changes from 1290.5 to 1288.3 eV going from ultrathin to thicker MgO layers. These two energies are characteristic of $4f^9$ and $4f^{10}$ electronic configurations, respectively, as deduced by comparison with previous data of Dy atoms on metals[11] and supported graphene.[4,12] The continuous evolution implies the coexistence of $4f^9$ and $4f^{10}$ Dy atoms, whose proportions depend on the MgO thickness.

https://doi.org/10.1021/acs.nanolett.1c02744
Nano Lett. 2021, 21, 8266−8273

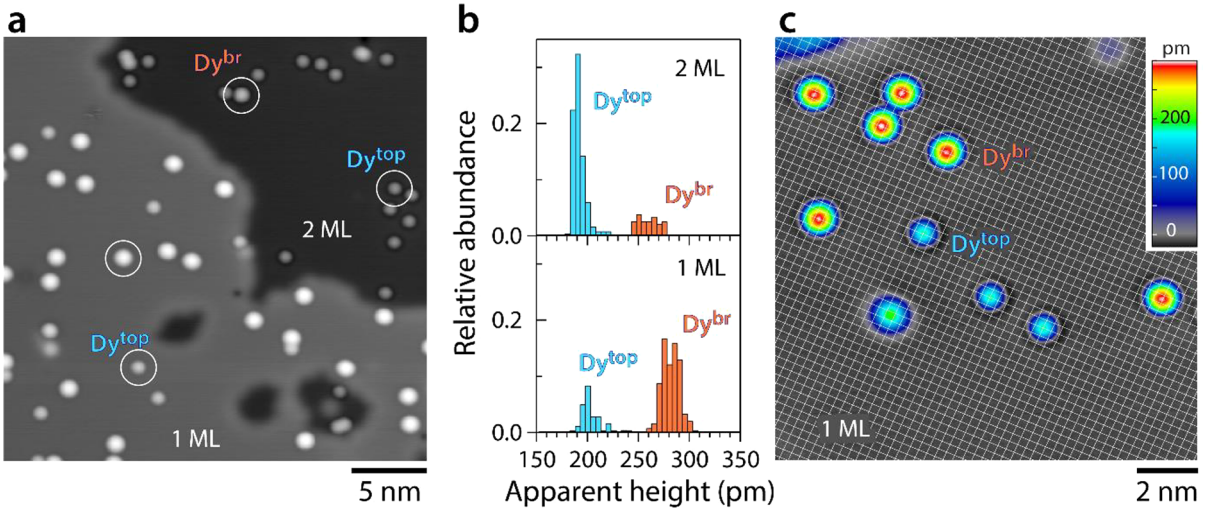

Figure 2. Scanning tunneling microscopy of Dy atoms on MgO/Ag(100). (a) After deposition on the MgO surface kept at around 10 K, two Dy species with different apparent heights are observed in STM images. (b) Apparent height distributions of the two Dy species for 1 and 2 ML MgO. (c) By overlapping a grid representative of the O sublattice, corresponding to the crossings of the grid, we identify the two species as Dy atoms adsorbed on O-top (Dy^{top}) and on bridge (Dy^{br}), respectively. The grid is obtained from an atomically resolved image of the MgO surface in a spot without Dy atoms. The species with elongated shape on the bottom-left side of the image is tentatively identified as a Dy dimer (Θ_{Dy} = 0.007 ML, V_t = −100 mV, I_t = 20 pA, T = 5 K).

In order to simulate the XAS/XMCD spectra and to derive quantitative information on the abundance of the different electronic configurations, we investigate the adsorption sites of Dy atoms using STM for the MgO thickness range accessible to this technique. On ultrathin MgO layers on Ag(100), Dy atoms appear as protrusions with two distinct apparent heights, whose precise values depend on the MgO layer thickness (see Figure 2a,b). Overlaying the MgO lattice deduced from atomic-resolution images allows one to attribute the 2-fold bridge adsorption site to the species with the largest apparent height and a 4-fold symmetric site to the other ones, see Figure 2c. Further samples prepared by codepositing Co and Dy allow one to ascertain the 4-fold adsorption site as O-top (see Figure S1).[3,35,36] The abundances of the two populations, hereafter being referred to as Dy^{br} and Dy^{top}, respectively, vary with the thickness of the MgO layer. On 1 ML MgO, Dy^{br} atoms (79 ± 4%) are more abundant than Dy^{top} ones (21 ± 4%), whereas on 2 ML thick regions the abundances are essentially reversed with 25 ± 5% Dy^{br} and 75 ± 5% Dy^{top}. A comparable ratio is also found on 3 ML MgO. This abrupt change of adsorption site abundances between 1 and 2 MgO layers seems dissociated from the smooth variation from $4f^9$ to $4f^{10}$ population occurring over a broader range of t_{MgO}, suggesting that the change in 4f occupation has a different origin. Similar variations in the relative population of O-top and bridge were also found for Ho atoms and ascribed to the layer-dependent transient mobility after surface adsorption.[35,36] However, compared to Ho, for the same MgO thickness Dy atoms show a larger abundance of bridge species[35,36] that need to be considered to interpret ensemble-averaged XAS/XMCD measurements.

To quantify the abundance of species with $4f^9$ and $4f^{10}$ configuration, we fit the angle-dependent XAS for each MgO thickness with simulated spectra from multiplet calculations using the MultiX code,[37] including the adsorption site specific C_{4v}- and C_{2v}-symmetric crystal field (CF) from a point charge model with the positions and values of the point charges deduced from DFT Born charges, as discussed in SI. Although the STM measurements are carried out on ultrathin MgO films, we assume that both adsorption sites are present also on thicker ones with both $4f^9$ and $4f^{10}$ occupations. This procedure provides us with spectra characteristic of each of the four electronic configuration−adsorption site pairs, which we combine to reproduce the experiments (see Figures S2 and S3). Our fits reproduce the angle-dependent XAS very well and provide the abundance of each species as a function of the thickness of the MgO film (Table S5) with the overall $4f^9$ and $4f^{10}$ fractions shown in Figure 1c. The $4f^9$ fraction changes smoothly from 84% for the thinnest MgO layer to 38% for the thickest one with the crossover between the two electronic configurations occurring at around 6−7 ML of MgO. The continuous trend is a consequence of the roughness of the MgO films on Ag(100).[38]

The ability to tune the electronic configuration by varying the MgO film thickness gives us the unique opportunity to characterize the magnetic properties of the Dy in $4f^9$ and $4f^{10}$ electronic states while keeping the same crystal field. Indeed, we observe a different magnetic behavior as highlighted by the angular and magnetic field dependence of the XMCD. The difference between normal and grazing incidence XMCD signals is almost negligible at the lowest MgO thickness where the $4f^9$ signal dominates, while it becomes more pronounced when the relative weight of the $4f^{10}$ configuration is larger, see Figure 1b.

Pronounced angular dependence of the XMCD with largest signal in normal incidence is the fingerprint of species with large perpendicular magnetic anisotropy.[3,4,11,12,17,18,21,34,39−41] The absence of out-of-plane anisotropy for the $4f^9$ species is in apparent contrast with previous STM studies finding record-high values of uniaxial perpendicular anisotropy for Dy^{top} on 2 ML MgO/Ag(100),[8] the largest among surface spins. However, due to $4f^9$ Dy^{br} atoms with a larger XMCD along the grazing orientation, the directional contribution of the two $4f^9$ species cancels out, resulting in a very small angular dependence of the overall $4f^9$ XMCD. On the other hand, the pronounced angular dependence at the $4f^{10}$ peak indicates that

https://doi.org/10.1021/acs.nanolett.1c02744
Nano Lett. 2021, 21, 8266−8273

both $4f^{10}$ Dy^{top} and Dy^{br} have perpendicular anisotropy, as also predicted by multiplet calculations (see Figure S2).

In order to evaluate the magnetic stability of the individual species, we acquire hysteresis loops by measuring the intensity of the XMCD while sweeping the external magnetic field. The energy difference in the XMCD peak related to the two electronic configurations allows one to resolve the field-dependent magnetization separately for the $4f^9$ and $4f^{10}$ species. Figure 3 shows the out-of-plane magnetization loops

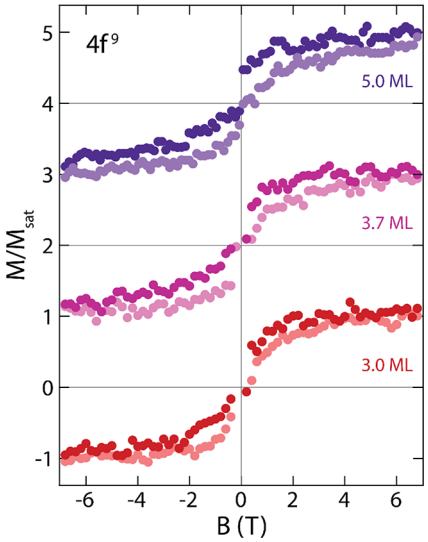

Figure 3. Out-of-plane hysteresis loops of Dy $4f^9$ species for different MgO thicknesses. The points represent the out-of-plane XMCD at the Dy $4f^9$ peak (1290.5 eV) acquired while sweeping the magnetic field at 33.3 mT/s (Θ_{Dy} = 0.009 − 0.014 ML, T = 2.5 K).

of the Dy $4f^9$ species acquired by measuring the XMCD signal at 1290.5 eV as a function of the magnetic field sweeping from +6.8 T to −6.8 T and back to +6.8 T with a rate of 33.3 mT/s. In all samples, we observe a narrow opening, which extends up to the maximum available field. The area of the loop slightly increases with the thickness of the MgO film, possibly due to a larger decoupling from the hot electrons generated in the Ag substrate by X-ray photon absorption.[42] The presence of magnetic hysteresis indicates that the magnetic relaxation to the ground state is slower than the time resolution of the experiment. According to previous STM results,[8] Dy^{top} atoms exhibit a long magnetic lifetime up to 5 T, which should result in a wide hysteresis loop. Conversely, Dy^{br} atoms, being in a low symmetry CF, are expected to show reduced magnetic lifetime and to exhibit a fully paramagnetic loop. On the basis of the mixed composition of the ensemble, we interpret the narrow hysteresis as an average behavior between hysteretic Dy^{top} and paramagnetic Dy^{br} species.

The out-of-plane hysteresis curve acquired at the XMCD peak of the $4f^{10}$ species (1288.3 eV) reveals a very different shape and pronounced anisotropy; see Figures 4a and S4. The loop is wide open up to 3 T with a strong signature of QTM at zero external field. Similar signature of QTM was also observed for Dy(II) $4f^95d^1$ in single ion magnets[22] and ascribed to the non-Kramers nature of the ion, which is more sensitive to deviations from a perfect axial environment.[31] The low symmetry adsorption geometry of the $4f^{10}$ Dy^{br} is not expected to enable long magnetic lifetimes, similar to $4f^9$ Dy^{br} discussed

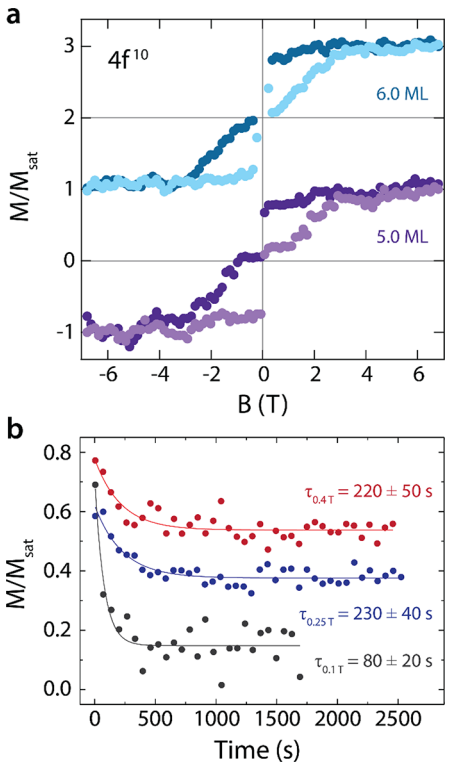

Figure 4. Out-of-plane hysteresis loops and magnetic relaxation of Dy $4f^{10}$ species. (a) The points represent the out-of-plane XMCD at the Dy $4f^{10}$ peak (1288.3 eV) acquired while sweeping the magnetic field at 33.3 mT/s for different MgO thicknesses. (b) Decay of the normal incidence XMCD signal as a function of time for B = 0.4 T (red dots), B = 0.25 T (blue dots), and B = 0.1 T (black dots) after saturating the ensemble at 3 T on a sample with 6.0 ML MgO. Lines are exponential fits to the data providing the magnetic lifetime τ at the related field (Θ_{Dy} = 0.009 − 0.012 ML, T = 2.5 K).

above. Hence, we attribute the hysteretic behavior of the $4f^{10}$ species to the Dy^{top} atoms.

To quantify the lifetime of the $4f^{10}$ Dy^{top}, we record the time decay of the XMCD signal at constant external field after saturating the magnetization in a field of 3 T prior to switching the field to the indicated values and starting the acquisition.[3,4,18,40,42,43] Figure 4b shows the magnetic relaxation at three different external fields with the asymptotic value of the XMCD signal indicating the corresponding equilibrium magnetization of the ensemble. The $4f^{10}$ species show a magnetic lifetime of about 200 s at both 0.25 and 0.4 T, while lowering the field to 0.1 T shortens the relaxation time to less than 100 s due to QTM becoming more effective in this field range, as observed for other non-Kramers single molecule magnets.[22] Magnetic relaxation at lower fields becomes too fast to be detected with our setup. The lifetime of $4f^{10}$ Dy atoms on MgO is a few orders of magnitude shorter than that reported for $4f^9$ Dy^{top} on 2 ML MgO/Ag(100),[8] and for other Ho and Dy single atom magnets with the same 4f occupation[3,12,43] but similar to that of divalent Dy $4f^95d^1$ single molecule magnets in polycrystalline form.[22]

In order to unravel the mechanism determining the variation of the Dy 4f orbital filling with the thickness of the supporting MgO layer, we perform DFT calculations using pseudopotentials and plane wave bases, as implemented in Quantum Espresso.[44−49] To correct for the self-interaction of the exchange-correlation functional, we applied a Hubbard U

https://doi.org/10.1021/acs.nanolett.1c02744
Nano Lett. 2021, 21, 8266−8273

correction of 9 eV on both the 4f and 5d manifolds.[50,51] To understand the role of the adsorption site and of the Ag(100) substrate, we simulate the Dy^{top} and Dy^{br} species on both free-standing 2 ML MgO(100) and 2 ML MgO/Ag(100). When adsorbed on O-top on MgO(100) (Figure 5a), the Dy atoms

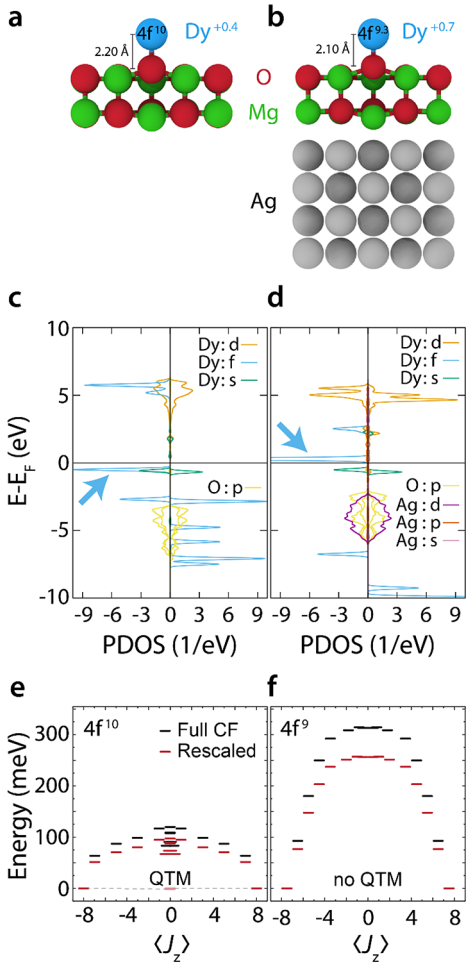

Figure 5. Calculated adsorption geometry, as well as electronic and magnetic configurations of Dy^{top} atoms. Cross section of the Dy/surface adsorption complex along the crystallographic (010) direction on (a) 2 ML free-standing MgO(100) and (b) 2 ML MgO/Ag(100), showing the charge state, 4f occupation, and Dy−O bond length. PDOS of Dy atoms on (c) MgO(100), and (d) MgO/Ag(100) obtained from DFT. The thick cyan arrows mark the 4f states that are mostly affected by the presence of the Ag(100) and determine the change of 4f occupation in Dy atoms. (e) Energy level scheme for the magnetic states of Dy atoms in the $4f^{10}$ configuration obtained from multiplet calculations using the structure calculated in (a). Dashed lines show the ground state mixing at zero field, producing two singlet states with no net magnetization (light red lines). (f) Energy level scheme for the magnetic states of the $4f^{9}$ configuration using the structure calculated in (b). In both (e,f), black lines are the result of the full CF potential, while red lines are obtained rescaling the CF by a factor 0.8 to match results of previous STM experiment.[8]

show an atomic-like $4f^{10}$ occupation, with a slight electron transfer of 0.4 *e* to the MgO, mostly from the outer 6s shell. Differently, on MgO/Ag(100) the presence of the Ag layer induces a reorganization of the electronic configuration to $4f^{9.3}$ with almost one electron transferred from the 4f orbitals to the Ag substrate (Figure 5b). The corresponding orbital-projected density of states (PDOS) of the Dy^{top} species reveals a different occupation of the 4f minority states close to the Fermi level, as highlighted in Figures 5c,d. When Dy is adsorbed on free-standing MgO, we observe a peak in the 4f PDOS below the Fermi level, which moves to the unoccupied states on MgO/Ag(100). Our calculations reveal that the reorganization of the 4f charge is driven by two factors: (i) more pronounced electron transfer from the Dy to the substrate when the Ag(100) is included (0.4 *e* for MgO, 0.7 *e* for MgO/Ag(100)), (ii) shortening of the bond length to the underneath O from 2.2 Å for MgO to 2.1 Å for MgO/Ag(100), as also indicated in Figure 5a,b, and Table S7. Remarkably, both the orbital occupation and bond length of Dy/MgO/Ag(100) are essentially identical to that of $[Dy/MgO]^+$, where the total charge of the system is artificially reduced by one unit (see SI). Very similar behavior is also observed in the calculations for the bridge site (see SI). This similarity suggests a simplified picture with the Dy atoms on MgO/Ag(100) assuming a singly ionized configuration and those on free-standing MgO films keeping a close to neutral state. As also observed for pentacene on MgO/Ag(100), the gradual neutralization of the charged species with increasing MgO thickness can be attributed to the increase of electrostatic energy as in an equivalent charged-capacitor scheme,[52] which progressively reduces the energy gain associated with the charging from the electron transfer. Using a plane capacitor model, we infer that an electrostatic energy of about 150 meV per Dy atom is required to overcome the configurational energy difference between $4f^9$ and $4f^{10}$ occupation, a value of comparable magnitude with respect to previous estimations for Dy divalent compounds.[15]

Changes in bond length and 4f occupation have a large impact on the adatom magnetic states and anisotropy barrier. For $4f^{10}$ Dy^{top}, multiplet calculations indicate a lowest manifold with total angular momentum $J = 8$ and relatively large level splitting of 120 meV, see Figure 5e. For these non-Kramers spins, the nonaxial crystal field terms generated by the nearest Mg neighbors mix the states of the lowest doublet with projected moment $J_z = \pm 8$ in a pair of nondegenerate singlets at zero magnetic field, resulting in QTM. Conversely, for the $4f^9$ Dy^{top} atoms we find a lowest manifold with $J = 15/2$ and giant anisotropy barrier of 314 meV, see Figure 5f. For these Kramers spins, the $J_z = \pm 15/2$ levels belonging to the lowest doublet cannot be mixed by crystal field terms due to time-reversal symmetry. Therefore, the ground state doublet is protected against QTM at zero magnetic field. The lack of QTM and the giant magnetic anisotropy identify the $4f^9$ Dy^{top} as an extremely stable quantum magnet, in agreement with previous findings.[8] Conversely, Dy^{br} species show strong mixing of the magnetic states due to the absence of axial symmetry (see Figure S7), hence lacking the prerequisite for magnetic stability. The apparent contradictory observation of a smaller opening in the magnetization curve of $4f^9$ vs $4f^{10}$ species originates from the fact that the $4f^9$ Dy^{top} lifetime is so long and weakly affected by the magnetic field that the spin dynamics is basically negligible in the time lapse of a hysteresis. Even in the presence of secondary electrons that can accelerate the dynamics of the spin state,[3,40,42] the $4f^9$ Dy^{top} population does not seem to attain a large imbalance between the two bistable spin orientations, hence the contribution to the $4f^9$ magnetization remains small. Consequently, the data on thin MgO films are dominated by the S-shaped curve of the paramagnetic $4f^9$ Dy^{br} atoms.

We finally note that the anisotropy barrier of $4f^9$ Dy^{top} predicted by our multiplet calculations is 25% larger than the

https://doi.org/10.1021/acs.nanolett.1c02744
Nano Lett. 2021, 21, 8266−8273

value of 258 meV (2081 cm^{-1}, 2994 K) inferred from STM experiments,[8] possibly due to the well-known inaccuracy of point charge models based on physical charge distribution.[53] By rescaling the CF charges of all species to match the previously reported barrier for $4f^9$ Dy^{top}, we obtain a reduced anisotropy barrier of 97 meV (782 cm^{-1}, 1126 K) for the $4f^{10}$ Dy^{top} (red lines in Figures 5e,f). For the latter species, the rescaled barrier height results are smaller than the one estimated for $4f^{10}$ Ho atoms on MgO[24,26] despite their identical 4f filling. The reason can be traced to the more extended Dy^{top}-O bond when Dy is in its neutral state, which reduces the uniaxial anisotropy component and hence the robustness of the magnetic states against QTM and spin-phonon scattering.[31]

Recent calculations for DyO linear complexes find anisotropy barriers of $4f^9$ and $4f^{10}$ electronic configurations comparable with our results.[31,32] The lower magnetic stability at zero field observed for the $4f^{10}$ Dy^{top} with respect to the previously reported long lifetime of $4f^{10}$ Dy/gr/Ir(111) is a consequence of the crystal field symmetry.[4,12] The adsorption on the graphene hollow site produces a C_{6v} symmetric CF resulting in a degenerate ground state doublet characterized by $J_z = 7$, and thus protected from QTM. On the contrary, in the present case, the C_{4v} symmetric CF produces a ground split-doublet exhibiting QTM in a vanishing magnetic field.

Electron transfer from metal supports through ultrathin MgO films has been observed for molecular adsorbates[52,54] and Au atoms.[36,54,55] The lower ionization potential of lanthanides offers the possibility to realize the opposite transfer mechanism, that is, from the adatom to the metal substrate. As shown in a previous study, such a mechanism occurs for Gd and Ho atoms, leaving the adsorbate in a singly ionized configuration.[24] Our findings reveal a very similar behavior for Dy: the charge transfer removes one electron from the 4f orbitals leading to a $4f^9$ occupation. In this configuration, adsorption on O-top gives rise to the highest magnetic anisotropy barrier observed for surface spins, and absence of QTM. Increasing the thickness of the oxide layer reduces the energy gain associated with this process,[52] inducing the Dy atoms to gradually recover a neutral atomic-like configuration. Although characterized by a reduced perpendicular anisotropy compared with the $4f^9$ Dy^{top} case, the $4f^{10}$ Dy^{top} species also exhibit long magnetic lifetimes and open hysteresis. Our results prove the charge transfer to be a controllable mechanism to tune the magnetic behavior in surface-adsorbed spins.

■ ASSOCIATED CONTENT

Supporting Information

The Supporting Information is available free of charge at https://pubs.acs.org/doi/10.1021/acs.nanolett.1c02744.

Sample preparation, STM and XAS/XMCD measurements, and the related analysis, additional details on the DFT and multiplet calculations (PDF)

■ AUTHOR INFORMATION

Corresponding Authors

Fabio Donati − *Center for Quantum Nanoscience, Institute for Basic Science (IBS), Seoul 03760, Republic of Korea; Department of Physics, Ewha Womans University, Seoul 03760, Republic of Korea;* orcid.org/0000-0002-3932-2889; Email: donati.fabio@qns.science

Stefano Rusponi − *Institute of Physics, École Polytechnique Fédérale de Lausanne, CH-1015 Lausanne, Switzerland;* orcid.org/0000-0002-8494-5532; Email: stefano.rusponi@epfl.ch

Authors

Marina Pivetta − *Institute of Physics, École Polytechnique Fédérale de Lausanne, CH-1015 Lausanne, Switzerland;* orcid.org/0000-0001-5330-8648

Christoph Wolf − *Center for Quantum Nanoscience, Institute for Basic Science (IBS), Seoul 03760, Republic of Korea; Ewha Womans University, Seoul 03760, Republic of Korea;* orcid.org/0000-0002-9340-9782

Aparajita Singha − *Center for Quantum Nanoscience, Institute for Basic Science (IBS), Seoul 03760, Republic of Korea; Ewha Womans University, Seoul 03760, Republic of Korea; Max Planck Institute for Solid State Research, 70569 Stuttgart, Germany*

Christian Wäckerlin − *Institute of Physics, École Polytechnique Fédérale de Lausanne, CH-1015 Lausanne, Switzerland; Surface Science and Coating Technologies, Empa - Swiss Federal Laboratories for Materials Research and Technology, 8600 Dübendorf, Switzerland;* orcid.org/0000-0001-6587-1235

Romana Baltic − *Institute of Physics, École Polytechnique Fédérale de Lausanne, CH-1015 Lausanne, Switzerland*

Edgar Fernandes − *Institute of Physics, École Polytechnique Fédérale de Lausanne, CH-1015 Lausanne, Switzerland*

Jean-Guillaume de Groot − *Institute of Physics, École Polytechnique Fédérale de Lausanne, CH-1015 Lausanne, Switzerland*

Safa Lamia Ahmed − *Center for Quantum Nanoscience, Institute for Basic Science (IBS), Seoul 03760, Republic of Korea; Department of Physics, Ewha Womans University, Seoul 03760, Republic of Korea*

Luca Persichetti − *Department of Materials, ETH Zurich, CH-8093 Zurich, Switzerland; Department of Sciences, Roma Tre University, I-00146 Roma, Italy;* orcid.org/0000-0001-6578-254X

Corneliu Nistor − *Department of Materials, ETH Zurich, CH-8093 Zurich, Switzerland*

Jan Dreiser − *Swiss Light Source (SLS), Paul Scherrer Institute (PSI), CH-5232 Villigen PSI, Switzerland;* orcid.org/0000-0001-7480-1271

Alessandro Barla − *Istituto di Struttura della Materia (ISM), Consiglio Nazionale delle Ricerche (CNR), I-34149 Trieste, Italy*

Pietro Gambardella − *Department of Materials, ETH Zurich, CH-8093 Zurich, Switzerland*

Harald Brune − *Institute of Physics, École Polytechnique Fédérale de Lausanne, CH-1015 Lausanne, Switzerland;* orcid.org/0000-0003-4459-3111

Complete contact information is available at: https://pubs.acs.org/10.1021/acs.nanolett.1c02744

Author Contributions

F.D., M.P., A.S., C.Wäckerlin, R.B., S.L.A., L.P., C.N., J.D., A.B., and S.R. performed the XAS/XMCD synchrotron experiments under the supervision of P.G. and H.B. The analysis of the XAS/XMCD data using multiplet calculations was performed by F.D. with the help of S.L.A. STM experiments were performed and analyzed by M.P., J.-G.de G., and E.F. DFT calculations were performed by C. Wolf. The

https://doi.org/10.1021/acs.nanolett.1c02744
Nano Lett. 2021, 21, 8266−8273

manuscript was written by F.D., M.P., C. Wolf, and S.R. and finalized through contributions of all authors. All authors have given approval to the final version of the manuscript.

Notes

The authors declare no competing financial interest.

■ ACKNOWLEDGMENTS

F.D, C. Wolf, A.S., and S.L.A. acknowledge support from the Institute for Basic Science under Grant IBS-R027-D1. C. Wäckerlin and J.D. acknowledge funding from SNF Ambizione through the Grant No. PZ00P2_142474.

■ ABBREVIATIONS

STM, scanning tunneling microscopy; XAS, X-ray absorption spectroscopy; XMCD, X-ray circular magnetic dichroism; t_{MgO}, average thickness of the MgO layer; Θ_{Dy}, Dy coverage; Dy^{top}, Dy atoms adsorbed on O-top site of MgO; Dy^{br}, Dy atoms adsorbed on bridge site of MgO; CF, crystal field; DFT, density functional theory; PDOS, projected density of states; QTM, quantum tunneling of the magnetization.

■ REFERENCES

(1) Goodwin, C. A. P.; Ortu, F.; Reta, D.; Chilton, N. F.; Mills, D. P. Molecular magnetic hysteresis at 60 K in dysprosocenium. *Nature* **2017**, *548* (7668), 439−442.

(2) Guo, F. S.; Day, B. M.; Chen, Y. C.; Tong, M. L.; Mansikkamaki, A.; Layfield, R. A. Magnetic hysteresis up to 80 K in a dysprosium metallocene single-molecule magnet. *Science* **2018**, *362* (6421), 1400−1403.

(3) Donati, F.; Rusponi, S.; Stepanow, S.; Wäckerlin, C.; Singha, A.; Persichetti, L.; Baltic, R.; Diller, K.; Patthey, F.; Fernandes, E.; Dreiser, J.; Sljivancanin, Z.; Kummer, K.; Nistor, C.; Gambardella, P.; Brune, H. Magnetic remanence in single atoms. *Science* **2016**, *352* (6283), 318−321.

(4) Baltic, R.; Pivetta, M.; Donati, F.; Wäckerlin, C.; Singha, A.; Dreiser, J.; Rusponi, S.; Brune, H. Superlattice of Single Atom Magnets on Graphene. *Nano Lett.* **2016**, *16* (12), 7610−7615.

(5) Ishikawa, N.; Sugita, M.; Ishikawa, T.; Koshihara, S.; Kaizu, Y. Lanthanide double-decker complexes functioning as magnets at the single-molecular level. *J. Am. Chem. Soc.* **2003**, *125* (29), 8694−8695.

(6) Dreiser, J. Molecular lanthanide single-ion magnets: from bulk to submonolayers. *J. Phys.: Condens. Matter* **2015**, *27* (18), 183203.

(7) Donati, F. Magnetic Relaxation Mechanisms in Ho Single Atom Magnets. *J. Magn.* **2020**, *25* (4), 441−452.

(8) Singha, A.; Willke, P.; Bilgeri, T.; Zhang, X.; Brune, H.; Donati, F.; Heinrich, A. J.; Choi, T. Engineering atomic-scale magnetic fields by dysprosium single atom magnets. *Nat. Commun.* **2021**, *12* (1), 4179.

(9) Thiele, S.; Balestro, F.; Ballou, R.; Klyatskaya, S.; Ruben, M.; Wernsdorfer, W. Electrically driven nuclear spin resonance in single-molecule magnets. *Science* **2014**, *344* (6188), 1135−8.

(10) Pedersen, K. S.; Ariciu, A. M.; McAdams, S.; Weihe, H.; Bendix, J.; Tuna, F.; Piligkos, S. Toward Molecular 4f Single-Ion Magnet Qubits. *J. Am. Chem. Soc.* **2016**, *138* (18), 5801−4.

(11) Singha, A.; Baltic, R.; Donati, F.; Wäckerlin, C.; Dreiser, J.; Persichetti, L.; Stepanow, S.; Gambardella, P.; Rusponi, S.; Brune, H. 4f-occupancy and magnetism of rare-earth atoms adsorbed on metal substrates. *Phys. Rev. B: Condens. Matter Mater. Phys.* **2017**, *96* (22), 224418.

(12) Baltic, R.; Donati, F.; Singha, A.; Wäckerlin, C.; Dreiser, J.; Delley, B.; Pivetta, M.; Rusponi, S.; Brune, H. Magnetic properties of single rare-earth atoms on graphene/Ir(111). *Phys. Rev. B: Condens. Matter Mater. Phys.* **2018**, *98* (2), 024412.

(13) Jaroschik, F.; Nief, F.; Le Goff, X.-F.; Ricard, L. Isolation of Stable Organodysprosium(II) Complexes by Chemical Reduction of Dysprosium(III) Precursors. *Organometallics* **2007**, *26* (5), 1123−1125.

(14) Moutet, J.; Schleinitz, J.; La Droitte, L.; Tricoire, M.; Pointillart, F.; Gendron, F.; Simler, T.; Clavaguéra, C.; Le Guennic, B.; Cador, O.; Nocton, G. Bis-Cyclooctatetraenyl Thulium(II): Highly Reducing Lanthanide Sandwich Single-Molecule Magnets. *Angew. Chem., Int. Ed.* **2021**, *60* (11), 6042−6046.

(15) Fieser, M. E.; MacDonald, M. R.; Krull, B. T.; Bates, J. E.; Ziller, J. W.; Furche, F.; Evans, W. J. Structural, Spectroscopic, and Theoretical Comparison of Traditional vs Recently Discovered Ln2+ Ions in the [K(2.2.2-cryptand)][(C5H4SiMe3)3Ln] Complexes: The Variable Nature of Dy2+ and Nd2+. *J. Am. Chem. Soc.* **2015**, *137* (1), 369−382.

(16) Nistor, C.; Mugarza, A.; Stepanow, S.; Gambardella, P.; Kummer, K.; Diez-Ferrer, J. L.; Coffey, D.; de la Fuente, C.; Ciria, M.; Arnaudas, J. I. Structure and magnetism of Tm atoms and monolayers on W(110). *Phys. Rev. B: Condens. Matter Mater. Phys.* **2014**, *90* (6), 064423.

(17) Donati, F.; Singha, A.; Stepanow, S.; Wäckerlin, C.; Dreiser, J.; Gambardella, P.; Rusponi, S.; Brune, H. Magnetism of Ho and Er atoms on close-packed metal surfaces. *Phys. Rev. Lett.* **2014**, *113* (23), 237201.

(18) Singha, A.; Donati, F.; Wäckerlin, C.; Baltic, R.; Dreiser, J.; Pivetta, M.; Rusponi, S.; Brune, H. Magnetic Hysteresis in Er Trimers on Cu(111). *Nano Lett.* **2016**, *16* (6), 3475−81.

(19) Guo, F. S.; Day, B. M.; Chen, Y. C.; Tong, M. L.; Mansikkamaki, A.; Layfield, R. A. A Dysprosium Metallocene Single-Molecule Magnet Functioning at the Axial Limit. *Angew. Chem., Int. Ed.* **2017**, *56* (38), 11445−11449.

(20) Ishikawa, N.; Sugita, M.; Okubo, T.; Tanaka, N.; Iino, T.; Kaizu, Y. Determination of Ligand-Field Parameters and f-Electronic Structures of Double-Decker Bis(phthalocyaninato)lanthanide Complexes. *Inorg. Chem.* **2003**, *42* (7), 2440−2446.

(21) Westerstrom, R.; Dreiser, J.; Piamonteze, C.; Muntwiler, M.; Weyeneth, S.; Brune, H.; Rusponi, S.; Nolting, F.; Popov, A.; Yang, S.; Dunsch, L.; Greber, T. An endohedral single-molecule magnet with long relaxation times: DySc2N@C80. *J. Am. Chem. Soc.* **2012**, *134* (24), 9840−3.

(22) Gould, C. A.; McClain, K. R.; Yu, J. M.; Groshens, T. J.; Furche, F.; Harvey, B. G.; Long, J. R. Synthesis and Magnetism of Neutral, Linear Metallocene Complexes of Terbium(II) and Dysprosium(II). *J. Am. Chem. Soc.* **2019**, *141* (33), 12967−12973.

(23) MacDonald, M. R.; Bates, J. E.; Fieser, M. E.; Ziller, J. W.; Furche, F.; Evans, W. J. Expanding Rare-Earth Oxidation State Chemistry to Molecular Complexes of Holmium(II) and Erbium(II). *J. Am. Chem. Soc.* **2012**, *134* (20), 8420−8423.

(24) Singha, A.; Sostina, D.; Wolf, C.; Ahmed, S. L.; Krylov, D.; Colazzo, L.; Gargiani, P.; Agrestini, S.; Noh, W.-S.; Park, J.-H.; Pivetta, M.; Rusponi, S.; Brune, H.; Heinrich, A. J.; Barla, A.; Donati, F. Orbital-resolved single atom magnetism measured with X-ray absorption spectroscopy. *ACS Nano* **2021**, DOI: 10.1021/acsnano.1c05026.

(25) MacDonald, M. R.; Bates, J. E.; Ziller, J. W.; Furche, F.; Evans, W. J. Completing the series of + 2 ions for the lanthanide elements: synthesis of molecular complexes of Pr2+, Gd2+, Tb2+, and Lu2+. *J. Am. Chem. Soc.* **2013**, *135* (26), 9857−68.

(26) Natterer, F. D.; Donati, F.; Patthey, F.; Brune, H. Thermal and Magnetic-Field Stability of Holmium Single-Atom Magnets. *Phys. Rev. Lett.* **2018**, *121* (2), 027201.

(27) Pivetta, M.; Patthey, F.; Di Marco, I.; Subramonian, A.; Eriksson, O.; Rusponi, S.; Brune, H. Measuring the Intra-Atomic Exchange Energy in Rare-Earth Adatoms. *Phys. Rev. X* **2020**, *10* (3), 031054.

(28) Natterer, F. D.; Yang, K.; Paul, W.; Willke, P.; Choi, T.; Greber, T.; Heinrich, A. J.; Lutz, C. P. Reading and writing single-atom magnets. *Nature* **2017**, *543* (7644), 226−228.

(29) Meihaus, K. R.; Fieser, M. E.; Corbey, J. F.; Evans, W. J.; Long, J. R. Record High Single-Ion Magnetic Moments Through $4f^n5d^1$

Electron Configurations in the Divalent Lanthanide Complexes $[(C_5H_4SiMe_3)_3Ln]^-$. *J. Am. Chem. Soc.* **2015**, *137* (31), 9855−60.
(30) Forrester, P. R.; Patthey, F.; Fernandes, E.; Sblendorio, D. P.; Brune, H.; Natterer, F. D. Quantum state manipulation of single atom magnets using the hyperfine interaction. *Phys. Rev. B: Condens. Matter Mater. Phys.* **2019**, *100* (18), 180405.
(31) Ungur, L.; Chibotaru, L. F. Strategies toward High-Temperature Lanthanide-Based Single-Molecule Magnets. *Inorg. Chem.* **2016**, *55* (20), 10043−10056.
(32) Zhang, W.; Muhtadi, A.; Iwahara, N.; Ungur, L.; Chibotaru, L. F. Magnetic Anisotropy in Divalent Lanthanide Compounds. *Angew. Chem., Int. Ed.* **2020**, *59* (31), 12720−12724.
(33) Piamonteze, C.; Flechsig, U.; Rusponi, S.; Dreiser, J.; Heidler, J.; Schmidt, M.; Wetter, R.; Calvi, M.; Schmidt, T.; Pruchova, H.; Krempasky, J.; Quitmann, C.; Brune, H.; Nolting, F. X-Treme beamline at SLS: X-ray magnetic circular and linear dichroism at high field and low temperature. *J. Synchrotron Radiat.* **2012**, *19*, 661−74.
(34) Westerstrom, R.; Uldry, A. C.; Stania, R.; Dreiser, J.; Piamonteze, C.; Muntwiler, M.; Matsui, F.; Rusponi, S.; Brune, H.; Yang, S.; Popov, A.; Buchner, B.; Delley, B.; Greber, T. Surface aligned magnetic moments and hysteresis of an endohedral single-molecule magnet on a metal. *Phys. Rev. Lett.* **2015**, *114* (8), 087201.
(35) Fernandes, E.; Donati, F.; Patthey, F.; Stavrić, S.; Šljivančanin, Ž.; Brune, H. Adsorption sites of individual metal atoms on ultrathin MgO(100) films. *Phys. Rev. B: Condens. Matter Mater. Phys.* **2017**, *96* (4), 045419.
(36) Fernandes, E. *Adsorption Sites of Metal Atoms on MgO Thin Films and Rotational Quantum State Spectroscopy of Physisorbed H_2*. Ph.D. Thesis No. 8144, EPFL, Lausanne, 2017.
(37) Uldry, A.; Vernay, F.; Delley, B. Systematic computation of crystal-field multiplets for x-ray core spectroscopies. *Phys. Rev. B: Condens. Matter Mater. Phys.* **2012**, *85* (12), 125133.
(38) Baumann, S.; Rau, I. G.; Loth, S.; Lutz, C. P.; Heinrich, A. J. Measuring the Three-Dimensional Structure of Ultrathin Insulating Films at the Atomic Scale. *ACS Nano* **2014**, *8* (2), 1739−1744.
(39) Studniarek, M.; Wäckerlin, C.; Singha, A.; Baltic, R.; Diller, K.; Donati, F.; Rusponi, S.; Brune, H.; Lan, Y.; Klyatskaya, S.; Ruben, M.; Seitsonen, A. P.; Dreiser, J. Understanding the Superior Stability of Single-Molecule Magnets on an Oxide Film. *Adv. Sci.* **2019**, *6* (22), 1901736.
(40) Wäckerlin, C.; Donati, F.; Singha, A.; Baltic, R.; Rusponi, S.; Diller, K.; Patthey, F.; Pivetta, M.; Lan, Y.; Klyatskaya, S.; Ruben, M.; Brune, H.; Dreiser, J. Giant Hysteresis of Single-Molecule Magnets Adsorbed on a Nonmagnetic Insulator. *Adv. Mater.* **2016**, *28* (26), 5195−9.
(41) Gambardella, P.; Rusponi, S.; Veronese, M.; Dhesi, S. S.; Grazioli, C.; Dallmeyer, A.; Cabria, I.; Zeller, R.; Dederichs, P. H.; Kern, K.; Carbone, C.; Brune, H. Giant Magnetic Anisotropy of Single Cobalt Atoms and Nanoparticles. *Science* **2003**, *300* (5622), 1130−1133.
(42) Dreiser, J.; Westerström, R.; Piamonteze, C.; Nolting, F.; Rusponi, S.; Brune, H.; Yang, S.; Popov, A.; Dunsch, L.; Greber, T. X-ray induced demagnetization of single-molecule magnets. *Appl. Phys. Lett.* **2014**, *105* (3), 032411.
(43) Donati, F.; Rusponi, S.; Stepanow, S.; Persichetti, L.; Singha, A.; Juraschek, D. M.; Wäckerlin, C.; Baltic, R.; Pivetta, M.; Diller, K.; Nistor, C.; Dreiser, J.; Kummer, K.; Velez-Fort, E.; Spaldin, N. A.; Brune, H.; Gambardella, P. Unconventional Spin Relaxation Involving Localized Vibrational Modes in Ho Single-Atom Magnets. *Phys. Rev. Lett.* **2020**, *124* (7), 077204.
(44) Giannozzi, P.; Baroni, S.; Bonini, N.; Calandra, M.; Car, R.; Cavazzoni, C.; Ceresoli, D.; Chiarotti, G. L.; Cococcioni, M.; Dabo, I.; Dal Corso, A.; de Gironcoli, S.; Fabris, S.; Fratesi, G.; Gebauer, R.; Gerstmann, U.; Gougoussis, C.; Kokalj, A.; Lazzeri, M.; Martin-Samos, L.; Marzari, N.; Mauri, F.; Mazzarello, R.; Paolini, S.; Pasquarello, A.; Paulatto, L.; Sbraccia, C.; Scandolo, S.; Sclauzero, G.; Seitsonen, A. P.; Smogunov, A.; Umari, P.; Wentzcovitch, R. M. QUANTUM ESPRESSO: a modular and open-source software project for quantum simulations of materials. *J. Phys.: Condens. Matter* **2009**, *21* (39), 395502.
(45) Giannozzi, P.; Andreussi, O.; Brumme, T.; Bunau, O.; Buongiorno Nardelli, M.; Calandra, M.; Car, R.; Cavazzoni, C.; Ceresoli, D.; Cococcioni, M.; Colonna, N.; Carnimeo, I.; Dal Corso, A.; de Gironcoli, S.; Delugas, P.; DiStasio, R. A.; Ferretti, A.; Floris, A.; Fratesi, G.; Fugallo, G.; Gebauer, R.; Gerstmann, U.; Giustino, F.; Gorni, T.; Jia, J.; Kawamura, M.; Ko, H. Y.; Kokalj, A.; Küçükbenli, E.; Lazzeri, M.; Marsili, M.; Marzari, N.; Mauri, F.; Nguyen, N. L.; Nguyen, H. V.; Otero-de-la-Roza, A.; Paulatto, L.; Poncé, S.; Rocca, D.; Sabatini, R.; Santra, B.; Schlipf, M.; Seitsonen, A. P.; Smogunov, A.; Timrov, I.; Thonhauser, T.; Umari, P.; Vast, N.; Wu, X.; Baroni, S. Advanced capabilities for materials modelling with Quantum ESPRESSO. *J. Phys.: Condens. Matter* **2017**, *29* (46), 465901.
(46) Dal Corso, A. Pseudopotentials periodic table: From H to Pu. *Comput. Mater. Sci.* **2014**, *95*, 337−350.
(47) Prandini, G.; Marrazzo, A.; Castelli, I. E.; Mounet, N.; Marzari, N. Precision and efficiency in solid-state pseudopotential calculations. *Npj Comput. Mater.* **2018**, *4* (1), 72.
(48) Blöchl, P. E. Projector augmented-wave method. *Phys. Rev. B: Condens. Matter Mater. Phys.* **1994**, *50* (24), 17953−17979.
(49) Perdew, J. P.; Burke, K.; Ernzerhof, M. Generalized Gradient Approximation Made Simple. *Phys. Rev. Lett.* **1996**, *77* (18), 3865−3868.
(50) Leiria Campo, V., Jr; Cococcioni, M. Extended DFT + U +Vmethod with on-site and inter-site electronic interactions. *J. Phys.: Condens. Matter* **2010**, *22* (5), 055602.
(51) Topsakal, M.; Wentzcovitch, R. M. Accurate projected augmented wave (PAW) datasets for rare-earth elements (RE = La-Lu). *Comput. Mater. Sci.* **2014**, *95*, 263−270.
(52) Hurdax, P.; Hollerer, M.; Puschnig, P.; Lüftner, D.; Egger, L.; Ramsey, M. G.; Sterrer, M. Controlling the Charge Transfer across Thin Dielectric Interlayers. *Adv. Mater. Interfaces* **2020**, *7* (14), 2000592.
(53) Goeller-Walrand, C.; Binnemans, K., Rationalization of Crystal-Field Parametrization. In *Handbook on the Physics and Chemistry of Rare Earths*; Gschneidner, K. A. J., Eyring, L., Eds.; Elsevier: Amsterdam, 1996; Vol. *23*, pp 121−283.
(54) Pacchioni, G.; Freund, H. Electron Transfer at Oxide Surfaces. The MgO Paradigm: from Defects to Ultrathin Films. *Chem. Rev.* **2013**, *113* (6), 4035−4072.
(55) Sterrer, M.; Risse, T.; Martinez Pozzoni, U.; Giordano, L.; Heyde, M.; Rust, H. P.; Pacchioni, G.; Freund, H. J. Control of the charge state of metal atoms on thin MgO films. *Phys. Rev. Lett.* **2007**, *98* (9), 096107.

https://doi.org/10.1021/acs.nanolett.1c02744
Nano Lett. 2021, 21, 8266−8273

Supplementary materials for "Correlation between electronic configuration and magnetic stability in dysprosium single atom magnets"

Fabio Donati[1,2,], Marina Pivetta[3], Christoph Wolf[1,4], Aparajita Singha[1,4,5], Christian Wäckerlin[3,6], Romana Baltic[3], Edgar Fernandes[3], Jean-Guillaume de Groot[3], Safa Lamia Ahmed[1,2], Luca Persichetti[7,8], Corneliu Nistor[7], Jan Dreiser[9], Alessandro Barla[10], Pietro Gambardella[7], Harald Brune[3], and Stefano Rusponi[3,*]*

[1]Center for Quantum Nanoscience, Institute for Basic Science (IBS), Seoul 03760, Republic of Korea

[2]Department of Physics, Ewha Womans University, Seoul 03760, Republic of Korea

[3]Institute of Physics, École Polytechnique Fédérale de Lausanne, Station 3, CH-1015 Lausanne, Switzerland

[4]Ewha Womans University, Seoul 03760, Republic of Korea

[5]Max Planck Institute for Solid State Research, Stuttgart, Germany

[6]Surface Science and Coating Technologies, Empa - Swiss Federal Laboratories for Materials Research and Technology, Überlandstrasse 129, 8600 Dübendorf, Switzerland

[7]Department of Materials, ETH Zurich, Hönggerbergring 64, CH-8093 Zurich, Switzerland

[8]Department of Sciences, Roma Tre University, I-00146, Roma, Italy

[9]Swiss Light Source (SLS), Paul Scherrer Institute (PSI), CH-5232 Villigen PSI, Switzerland

[10]Istituto di Struttura della Materia (ISM), Consiglio Nazionale delle Ricerche (CNR), I-34149 Trieste, Italy

Corresponding Authors

*donati.fabio@qns.science, stefano.rusponi@epfl.ch

1. Experimental details

A. Sample preparation.

Single crystals of Ag(100) were prepared by repeated cycles of sputtering and subsequent annealing to 773 K. For the XAS/XMCD experiments, MgO films with thickness between 2.5 and 9.0 monolayers (MLs) were grown by thermal evaporation of Mg in O_2 partial pressure of 1×10^{-6} mbar, with the substrate kept at 623 K and a Mg flux yielding a growth rate of about 0.2 ML/min. One monolayer is defined as one MgO(100) unit cell per Ag(100) substrate atom. The calibration of the MgO thickness was performed by measuring the Mg XAS K edge and comparing it to previous results.[1] The MgO/Ag(100) samples were transferred to the measurement position without breaking the vacuum. Dysprosium atoms were deposited from thoroughly degassed rods (purity 99 %), directly onto the substrate held at less than 10 K and in a base pressure of 2×10^{-11} mbar. Also for Dy, we define 1 ML as one lanthanide atom per Ag(100) substrate atom, and calibrate the amount by comparison with former experiments.[1]

For the STM experiments, MgO films with nominal thickness between 1 and 3 MLs were grown by thermal evaporation of Mg in O_2 partial pressure of 1×10^{-6} mbar, with the substrate kept at 750 K. Different MgO thicknesses coexist on the same sample and are identified by differential conductance spectroscopy.[2, 3] Dysprosium atoms were deposited from thoroughly degassed rods (purity 99 %), directly onto the substrate held at 10 K and in a base pressure of 1×10^{-10} mbar. The Dy coverage is determined by counting the number of adatoms in a given surface area.

B. XAS/XMCD measurements.

The XAS and XMCD measurements were performed at the EPFL/PSI X-Treme beamline at the Swiss Light Source.[4] The endstation is equipped with an ultra-high vacuum chamber for sample preparation (base pressure 5×10^{-10} mbar) and an Omicron variable-temperature scanning tunneling microscope (VT-STM). All measurements were performed with circularly polarized light in the total electron yield mode at sample temperatures of T = 2.5 K, and in external magnetic fields up to B = 6.8 T parallel to the x-ray beam. In order to isolate the contribution of the Dy atoms from the background signal, spectra of bare MgO/Ag(100) over the Dy $M_{4,5}$ edge are recorded for each sample prior to Dy deposition and subtracted from the final spectra. Hysteresis loops and magnetic relaxations were obtained by acquiring the XAS signal for the two circular polarizations at the XMCD peak corresponding to the 4f occupation of interest, 1290.5 eV for $4f^9$ and 1288.3 eV for $4f^{10}$, respectively. For the hysteresis loops, the field-evolution of the two polarizations has been acquired separately in two subsequent loops. For the magnetic relaxation, XAS signal at alternating polarization was acquired as a function of time after saturating the ensemble to B = +3 T. During the sweep of the magnetic field from the saturating to the measurement value, the beam shutter was kept closed to prevent undesired photon-induced relaxation. In this way, the ensemble is largely preserved in its saturated state until the beginning of the measurement. For both hysteresis

and relaxation measurements, the XAS from the two opposite polarizations was normalized to the corresponding pre-edge signal measured at 1281.3 eV, also acquired in the same sequence, to compensate for any spurious variation of the beam intensity during the acquisition. In order to minimize the influence of the photon beam on the lifetime of the magnetic atoms,[5] all the measurements were performed at the smallest photon flux ensuring a sufficient signal to noise ratio. For spectra and hysteresis loops, we used $\phi = 0.55 \times 10^{-2}$ nm^{-2} s^{-1}, while for relaxation curves $\phi = 0.14 \times 10^{-2}$ nm^{-2} s^{-1}.[1, 5]

C. STM measurements.

STM measurements were performed with a home-built STM at 5 K using W tips. The STM images were acquired in constant-current mode with the tunnel voltage applied to the sample.

2. Identification of the adsorption sites of Dy atoms

We determine the adsorption site of the Dy species by co-evaporating Dy and Co, as the latter, adsorbing on O-top site, acts as a marker for O lattice positions.[1-3] Figure S1 shows a 2 ML MgO region with co-evaporated Dy and Co. The overlaid MgO lattice, with white (black) dots representing oxygen (magnesium) atoms, is extracted from atomically resolved images of the MgO substrate. By aligning the white dots (O atoms) with the Co adatoms, one observes that the Dy adatoms with lower apparent height are adsorbed on O-top sites, while the species with higher apparent height adsorb on bridge sites. Hence, we identify the former as Dy^{top} and the latter as Dy^{br}.

The change in abundance of Dy^{top} and Dy^{br} species between the first and second layer has been previously observed for Ho,[1, 2] Tb, and Er.[3] The neat change in the favored adsorption site is mostly due to the MgO thickness dependent energy associated with the bonding formation and structural distortion resulting in a modified position of the MgO surface atoms. The adsorption on the bridge site allows the formation of a double bond with the surface oxygen which lowers the energy of the system. However, such a bonding configuration requires a more pronounced structural distortion of the MgO surface, which becomes less favorable as the thickness of the MgO film increases due to the increase of the stiffness of the MgO structure. Therefore, adsorption on bridge site becomes less favorable already starting from 2 ML MgO.[2, 3]

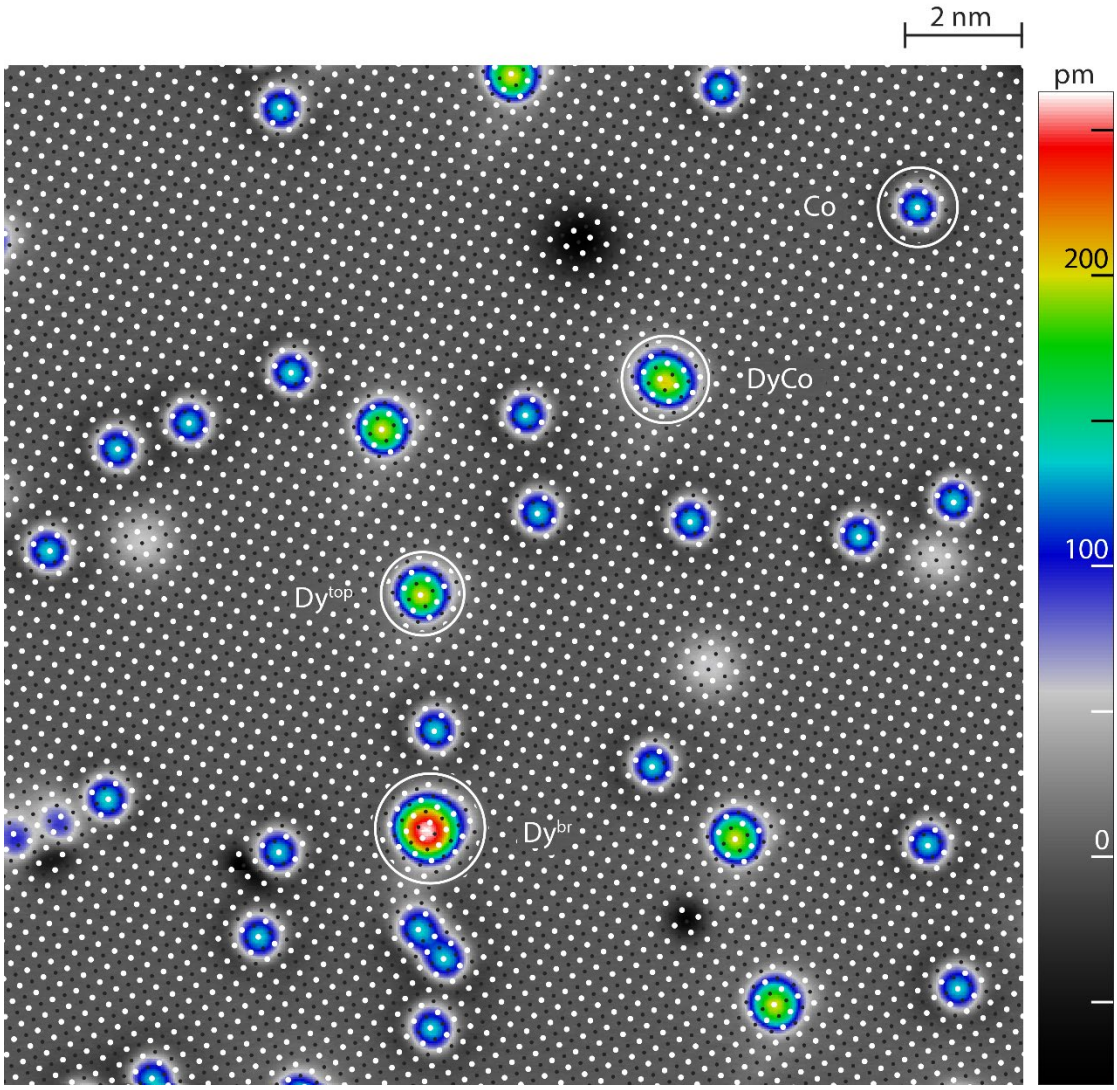

Figure S1. Identification of the adsorption site of Dy atoms. STM image of co-deposited Dy and Co on 2 ML MgO/Ag(100). The MgO lattice is extracted from atomically resolved images of the substrate. The white dots, representing the O atoms of the MgO lattice, are brought into coincidence with the Co adatoms. The black dots correspond to the position of Mg atoms. An elongated object is identified as a DyCo heterodimer. (V_t = -100 mV, I_t = 20 pA, T_{STM} = 5 K).

3. Details of multiplet calculations

XAS and XMCD spectra of the individual species have been calculated using the MultiX code.[6] The electron-electron interaction has been rescaled by 0.80 and 0.75 for Dy $4f^9$ and $4f^{10}$, respectively, to match the spectral shape observed in experiments. A core-hole broadening of 0.6 eV gave best match with the data linewidth. For the different species, we simulated spectra using a point charges model. The position and intensity of the nearest neighbors' charges have been obtained from DFT, with the intensity provided in terms of Born effective charges. For the Dy $4f^9$ species, we used the coordinates obtained for Dy on MgO/Ag(100), while for Dy $4f^{10}$ species we adopted the structure calculated for the Dy atoms on bare MgO (see Sec. S6). The position and intensity of the point charges are reported in Tables 1-4.

As mentioned in the text, the use of Born effective charges gives a level splitting for $4f^9$ Dy^{top} that overestimates previous values of spin-switching thresholds from STM experiments,[7] with a 0.8 rescaling factor on the intensities required to match the reported values. Due to the large energy splitting, this rescaling does not affect the shape of the XAS and XMCD spectra, which mostly reflects the population of the lowest states. On the other hand, the Löwdin analysis gives charge intensities about 50% smaller than the Born values, leading to large underestimation of the level splitting. Although the optimal charge values seem to lie in between the two analyses, the Born charges provide a better approximation to the effective crystal field generated by the Mg and O ions.

Table S1. Point charge crystal field for $4f^9$ Dy^{top} atoms. Coordinates (X,Y,Z) are provided in Å, while the charge intensity Q is given in multiples of electron charge.

Element	X	Y	Z	Q
O	0.000	0.000	-2.012	-2
O	-2.072	-2.072	-2.732	-2
O	-2.072	2.072	-2.732	-2
O	2.072	2.072	-2.732	-2
O	2.072	-2.072	-2.732	-2
Mg	-2.143	0.000	-2.771	2
Mg	0.000	2.143	-2.771	2
Mg	2.143	0.000	-2.771	2
Mg	0.000	-2.143	-2.771	2

Table S2. Point charge crystal field for $4f^9$ Dy^{br} atoms. Coordinates (X,Y,Z) are provided in Å, while the charge intensity Q is given in multiples of electron charge.

Element	X	Y	Z	Q
O	-0.994	-0.994	-1.739	-2
O	0.994	0.994	-1.739	-2
Mg	-1.114	1.114	-2.451	2
Mg	1.114	-1.114	-2.451	2

Table S3. Point charge crystal field for $4f^{10}$ Dy^{top} atoms. Coordinates (X,Y,Z) are provided in Å, while the charge intensity Q is given in multiples of electron charge.

Element	X	Y	Z	Q
O	0.000	0.000	-2.204	-2
O	-2.077	-2.077	-2.714	-2
O	-2.077	2.077	-2.714	-2
O	2.077	2.077	-2.714	-2
O	2.077	-2.077	-2.714	-2
Mg	-2.134	0.000	-2.729	2
Mg	-0.000	2.134	-2.729	2
Mg	2.134	0.000	-2.729	2
Mg	0.000	-2.134	-2.729	2

Table S4. Point charge crystal field for $4f^{10}$ Dy^{br} atoms. Coordinates (X,Y,Z) are provided in Å, while the charge intensity Q is given in multiples of electron charge.

Element	X	Y	Z	Q
O	-0.981	-0.981	-2.020	-2
O	0.981	0.981	-2.020	-2
Mg	-1.115	1.115	-2.503	2
Mg	1.115	-1.115	-2.503	2

Corresponding simulated XAS and XMCD spectra of the 4 species are shown in Fig. S2. For all species, the normal and grazing incidence spectra are calculated with the magnetic field and photon beam parallel to and at 60 degrees from the surface normal, respectively. For the bridge species, the magnetic field and photon axis in grazing incidence are oriented at an azimuth angle of 45 degrees with respect to the O-Dy-O bond. Except for the $4f^9$ Dy^{br}, all species show pronounced angular dependence of the XAS and perpendicular magnetic anisotropy. Conversely, $4f^9$ Dy^{br} show a strong in-plane anisotropy. The presence of two $4f^9$ species with opposite anisotropy results in a negligible XMCD angular dependence for $t_{MgO} < 4$ ML since, for these thicknesses, the signal is largely dominated by the two $4f^9$ species, as discussed in the main text.

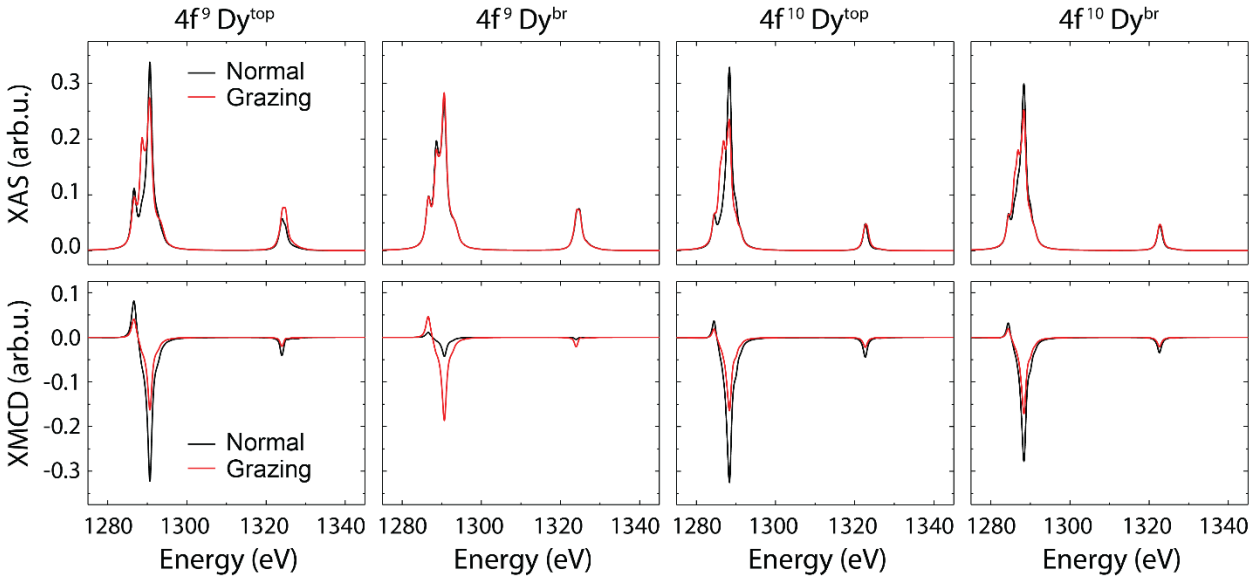

Figure S2. Simulated spectra for the four Dy species calculated for normal (black lines) and grazing incidence (red lines) for an applied field B = 6.8 T and a temperature T = 2.5 K.

4. Fit of the XAS spectra

The simulated XAS of the 4 species shown in Fig. S2 have been used to identify the composition of the ensemble. As also pointed out for the case of Ho atoms on MgO,[8, 9] the very long magnetic lifetime of $4f^9$ Dy^{top} at large fields does not allow the ensemble to attain magnetic saturation, resulting in reduced intensity of XMCD. Due to this effect, it is not possible to perform a correct fit of the XMCD using simulated spectra from multiplet calculations. On the other hand, XAS spectra are essentially insensitive to the magnetization of the ensemble, allowing meaningful comparison with simulations. The use of only XAS spectra in the fitting procedure allows us to reliably distinguish species with different 4f occupation due to the large difference in the spectral shape between $4f^9$ and $4f^{10}$, see Fig S2. On the other hand, the precision of the individual adsorption site abundance is expected to be low as the differences between XAS spectra of atoms with the same 4f occupation are not very pronounced.

For every MgO thickness, simultaneous fit of the normal and grazing incidence XAS was used to identify the amount of $4f^9$ vs. $4f^{10}$ species. Results of the individual fitting are shown in Fig. S3. The relative abundance of the Dy $4f^9$ and $4f^{10}$ species as a function of the MgO thickness are summarized in Table S5. Summed values for each 4f occupation from the same table are plotted in Fig. 1c of the main text.

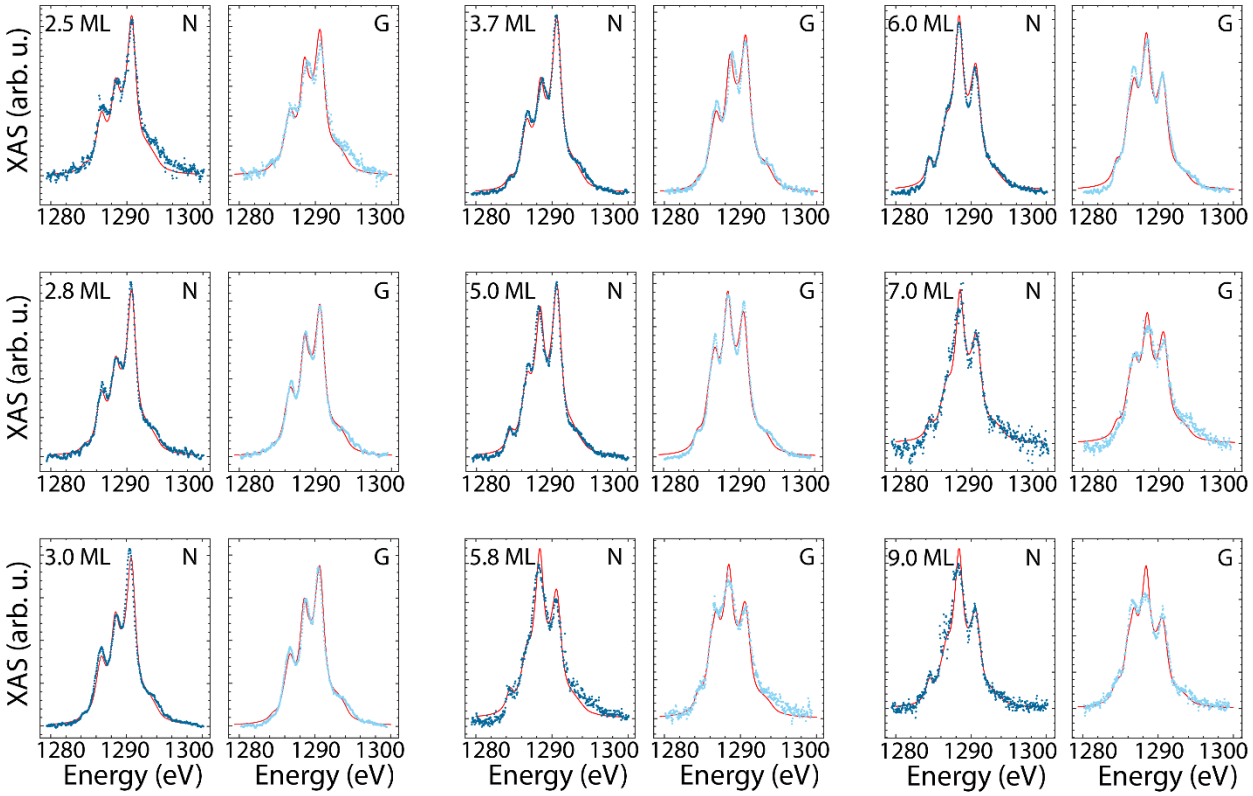

Figure S3. Individual fit of the experimental XAS performed using simulated spectra from multiplets. For every spectrum, the panels show the corresponding MgO thickness in ML and the sample orientation with respect to the field (N normal incidence, G grazing incidence).

Table S5. Abundance of Dy species considered in the fit using calculated spectra from multiplet calculations. Shown are also the summed abundance of $4f^9$ and $4f^{10}$ occupations plotted in Fig. 1c of the main text.

t_{MgO} (ML)	$4f^9$ Dy^{top}	$4f^9$ Dy^{br}	$4f^{10}$ Dy^{top}	$4f^{10}$ Dy^{br}	Sum $4f^9$	Sum $4f^{10}$
2.5	45 ± 3 %	39 ± 3 %	7 ± 6 %	9 ± 7 %	84 ± 4 %	16 ± 4 %
2.8	47 ± 1 %	38 ± 1 %	10 ± 2 %	5 ± 3 %	84 ± 2 %	16 ± 2 %
3.0	32 ± 2 %	52 ± 2 %	0 ± 3 %	16 ± 4 %	84 ± 2 %	16 ± 2 %
3.7	48 ± 1 %	29 ± 2 %	12 ± 3 %	11 ± 3 %	77 ± 2 %	23 ± 2 %
5.0	52 ± 1 %	6 ± 1 %	33 ± 2 %	9 ± 3 %	58 ± 2 %	42 ± 2 %
5.8	27 ± 3 %	20 ± 3 %	43 ± 6 %	45 ± 7 %	47 ± 4 %	53 ± 4 %
6.0	27 ± 1 %	18 ± 1 %	44 ± 3 %	11 ± 3 %	45 ± 2 %	55 ± 2 %
7.0	6 ± 3 %	47 ± 3 %	27 ± 6 %	20 ± 7 %	53 ± 4 %	47 ± 4 %
9.0	21 ± 2 %	17 ± 2 %	31 ± 5 %	31 ± 6 %	38 ± 3 %	62 ± 3 %

5. Anisotropy of the hysteresis loops

As discussed in the main text, XMCD spectra of ensembles with large majority of $4f^9$ species show very little angular dependence. In line with this finding, hysteresis loops acquired at the $4f^9$ peak of the XMCD spectra also show negligible angular dependence, with minor narrowing of the hysteresis area in grazing incidence, see Fig. S4. As discussed, we attribute this lack of angular dependence to the dominant contribution of the two $4f^9$ species with opposite anisotropy.

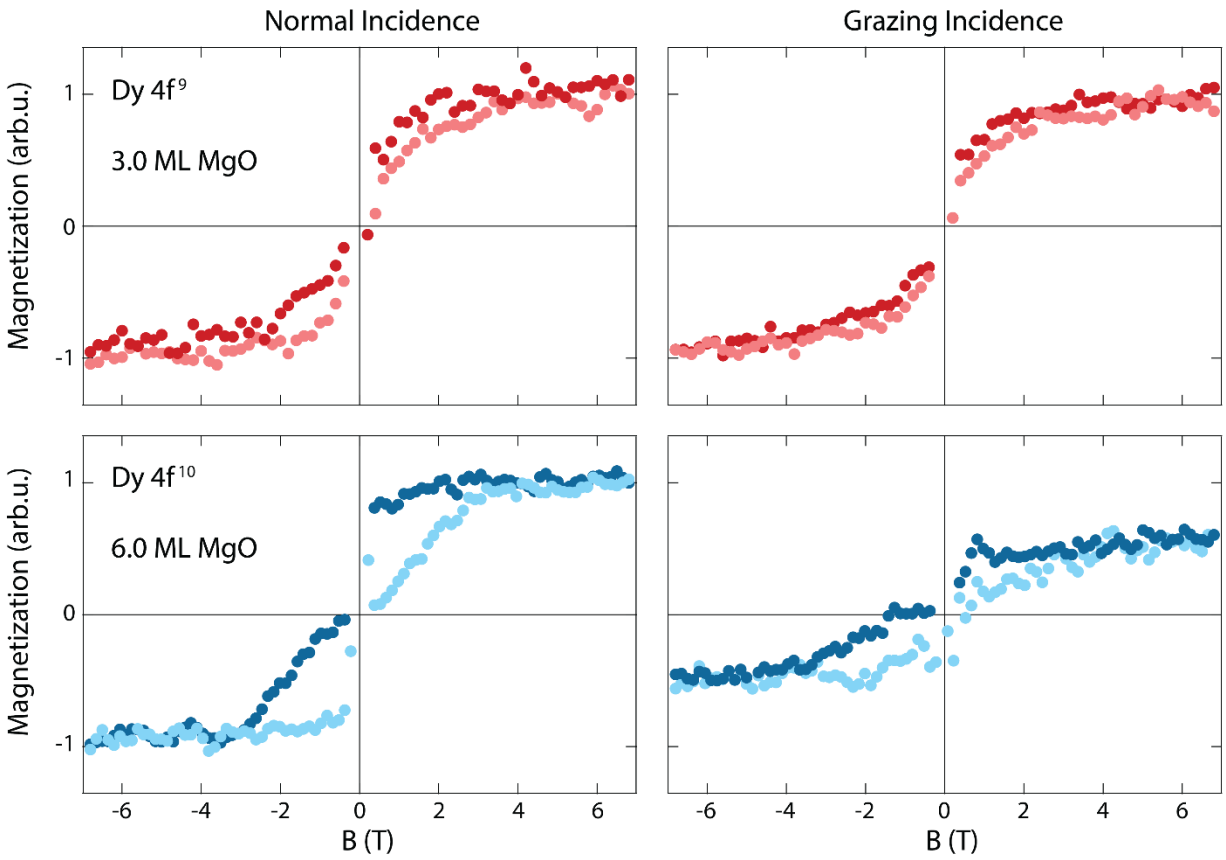

Figure S4. Angular dependent hysteresis loops acquired at the $4f^9$ (top panels) and $4f^{10}$ peaks (bottom panels) for two different samples.

Conversely, ensembles with majority of $4f^{10}$ species show stronger XMCD signal at normal incidence. Accordingly, the spectra acquired at the corresponding peak show larger magnetization along the normal incidence. We attribute this behavior to the fact that both $4f^{10}$ species show perpendicular anisotropy, see Fig. S2.

6. Details of DFT calculations

To investigate the adsorption geometry and electronic configuration of Dy on thin layers of MgO, we performed density functional theory (DFT) calculations using pseudopotentials and plane wave bases as implemented in Quantum Espresso.[10, 11] The system setup consists of 4 monolayers (ML) of silver exposing the (100) surface expanded into a 3x3 lateral supercell capped by 2 ML of MgO and 15 Å of vacuum. Dy is placed on top of either oxygen or a bridge site and the system was relaxed until the residual forces were less than 10^{-3} Ry/a_0 (a_0 is the Bohr radius). Highly localized electronic manifolds such as the f-shell and d-shell are prone to systematic errors due to self-interaction of the exchange-correlation functional leading to fractional electron occupations. To correct for this we applied a Hubbard U correction of 9 eV on the 4f and 5d manifolds, which drastically improves the occupations of the respective shells.[12, 13] Pseudopotentials were chosen according to the SSSP efficiency table except for the silver pseudopotential which was taken from the PSL library (version 0.3.1) expanded into plane waves using a kinetic cutoff of 40 Ry and a cutoff for the charge density of 400 Ry.[14, 15] All pseudopotentials use the projector augmented wave (PAW) method and the Perdew-Burker-Enzerhofer (PBE) parametrization for the exchange-correlation potential.[16, 17] The Brillouin zone was sampled using a 3x3x1 Monkhorst-Pack grid and we apply a smearing of about 160 K for the electronic states. We find that the magnetic states of the Dy are not affected by the k-point sampling beyond the chosen grid nor the electronic broadening between 16 and 1000 K as they are basically non-dispersive.

For the case of MgO/Ag(100), we find, in good approximation, a singly charged Dy for both adsorption sites with 4f occupancy close to $4f^9$. We note that the substrate plays an important role

in lowering the energy of the 6s states relative to the 4f states, as a singly charged Dy in vacuum would adopt a $6s^1 4f^{10}$ configuration based on our calculations. The results are summarized in Table S5. Also shown in Table S6 is the spin polarization (the difference between up and down Löwdin charges), which is almost completely due to the 4f electrons, while only negligible amount is localized on the valence 5d6s orbitals.

Table S6. Calculated electronic configuration of Dy atoms on MgO and MgO/Ag(100). The polarization is calculated as the difference between majority and minority Löwdin charges (n_{up}-n_{down}) for the indicated orbitals. The free-atom configuration is provided as reference.

Site	**Substrate**	**Dy charge**	**Configuration**	**Polarization**
-	Free atom	+0.0 e	$4f^{10.0}\,6s^{2.0}\,5d^{0.0}$	$4f^{5.0}6s^{0.0}5d^{0.0}$
Top	MgO/Ag(100)	+0.7 e	$4f^{9.3}\,6s^{1.5}\,5d^{0.4}$	$4f^{4.7}6s^{0.0}5d^{0.0}$
Top	MgO	+0.4 e	$4f^{10}\,6s^{1.5}\,5d^{0.2}$	$4f^{3.9}6s^{0.0}5d^{0.0}$
Bridge	MgO/Ag(100)	+0.6 e	$4f^{9.1}\,6s^{1.3}\,5d^{1.1}$	$4f^{4.9}6s^{0.3}5d^{0.2}$
Bridge	MgO	+0.4 e	$4f^{10.0}\,6s^{1.2}\,5d^{0.2}$	$4f^{4.0}6s^{0.0}5d^{0.0}$

To study the co-existence of different charge states we remove the silver and thereby the ability of the Dy to give a charge to the metal support substrate. We then remove one electron from the entire system which we denote as $[MgO]^{+1}$, which in excellent agreement reproduces the electronic configuration of Dy on MgO/Ag(100). By restoring the neutral cell ($[MgO]^{+0}$) we find a close to $6s^2 4f^{10}$ electronic configuration, indicating that a neutral species exists when the charge transfer to the metal substrate is suppressed by sufficiently thick MgO layers. The resulting density of states (DOS) projected onto atomic states is shown for each system in Fig. S5. Additional calculations

for the bridge absorption site (see Table S6 and Fig. S6) give similar results indicating that for thin layers of MgO a close to $6s^2 4f^9$ electronic configuration corresponding to a formal Dy^{+1} is adopted.

Consecutive relaxations of the system after removing the Ag layer have not shown any instabilities of these very thin layers. We further confirm the stability of the free-standing MgO layer by comparison with calculated Dy on 4 ML MgO. The change in geometry when increasing the MgO layer thickness is less than 0.02 Å for the Dy^{top}, indicating very minor differences with respect to the free-standing 2 ML MgO substrate, see Table S7.

Table S7. Calculated charge state and atomic distances between Dy and underneath O ($d_{Dy\text{-}O}$), neighboring Mg ($d_{Dy\text{-}Mg}$), and relative height with respect to the MgO surface for different substrates.

	Charge state	**$d_{Dy\text{-}O}$ (Å)**	**$d_{Dy\text{-}Mg}$ (Å)**	**h_{Dy} (Å)**
2 ML MgO/Ag(100)	+0.6 e	2.1015	3.5031	2.821
2 ML MgO	+0.4 e	2.2041	3.4640	2.762
4 ML MgO	+0.4 e	2.225	3.452	2.737

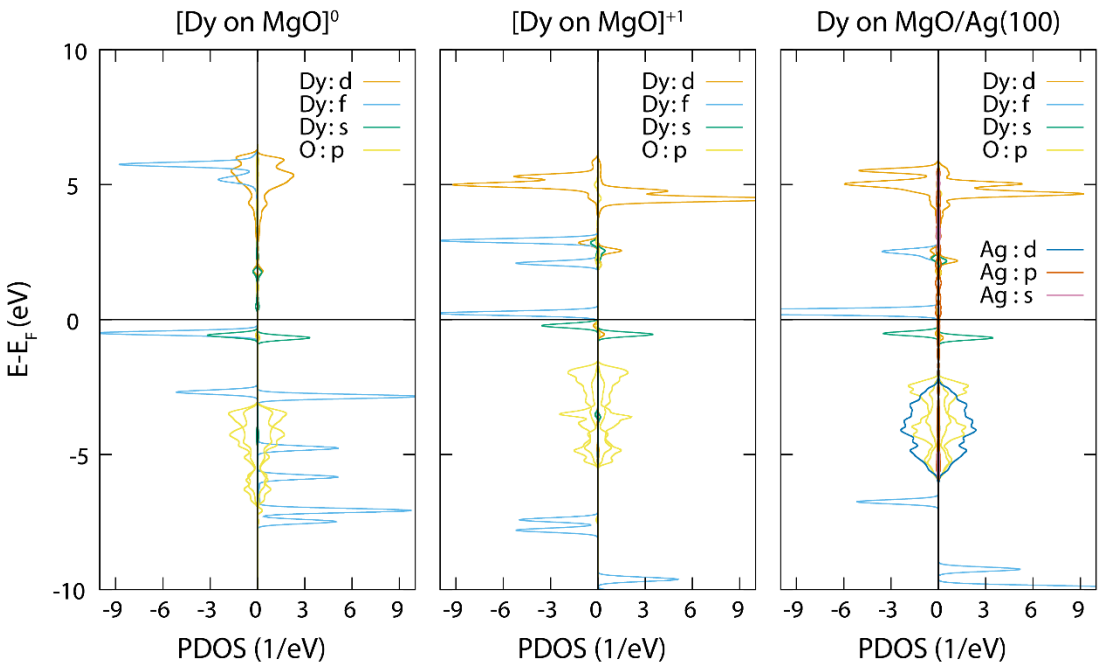

Figure S5. PDOS of Dy^{top} calculated for adsorption on O-top site of MgO for neutral and charged slab, as well as for MgO/Ag(100).

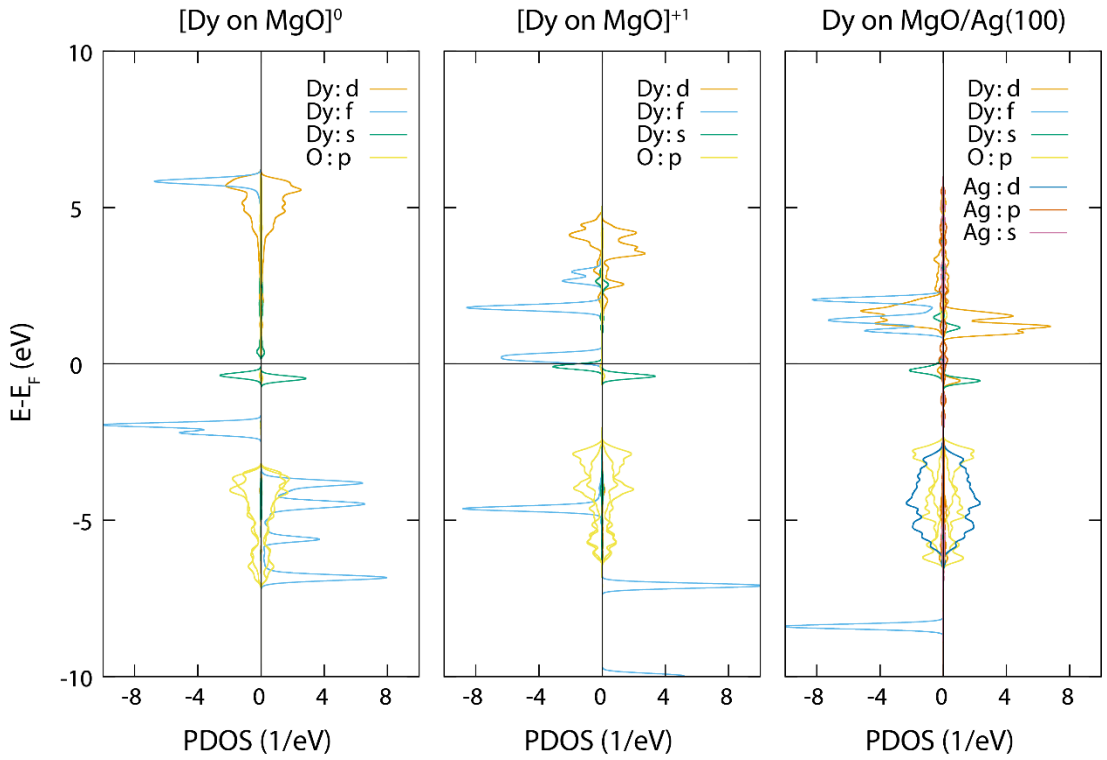

Figure S6. PDOS of Dy^{br} calculated for adsorption on bridge site of MgO for neutral and charged slab, as well as for MgO/Ag(100).

7. Quantum levels of Dy at the bridge site

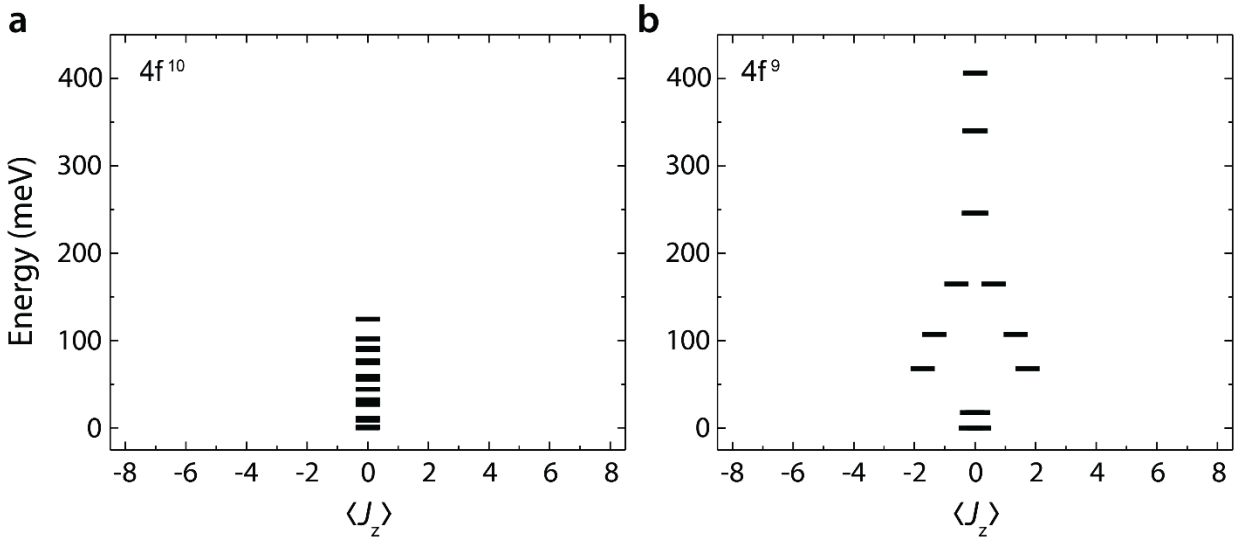

Figure S7. (a) Quantum levels of $4f^{10}$ Dy^{br} and $4f^{9}$ Dy^{br} obtained from multiplet calculations.

8. Model for electrostatic energy at the oxide layer

For lanthanide atoms, the occupation of 4f orbitals is generally dictated by the balance between atomic energy to promote one electron from the 4f to the outer shells and the energy gain in bonding formation/charge transfer to the substrate.[18] In the case of Dy atoms on MgO/Ag(100), the energy gain related to the charge transfer to the substrate and the stronger bond formation overcomes the configurational energy penalty required for the atoms to change from the neutral atomic $4f^{10}$ to the bulk-like $4f^{9}$ configuration. Hence, the configuration with singly ionized $4f^{9}$ species is attained, as shown by our DFT calculations. However, the thickness of the oxide layer provides another source of electrostatic energy cost that increases with the thickness of the dielectric. Above a critical thickness, the electrostatic energy becomes too large and makes both the charge transfer to the substrate and related $4f^{9}$ configuration unfavorable. Using a simple plane capacitor model, we estimate the additional electrostatic energy induced by the charged $4f^{9}$ atoms at the surface of the MgO film as $E = \frac{1}{2C} q^2$, with C being the capacity of the dielectric film and q the total charge at the surface. Using quantities defined per unit of area (A), such as $c = \frac{C}{A} = \epsilon_0 \epsilon_r / (t_{MgO}\, a_{MgO})$ and $\sigma = \frac{q}{A} = e\, n_{Dy}$, we obtain a surface energy density $\varepsilon = \frac{E}{A} = \frac{e^2\ a_{MgO}}{2\epsilon_0 \epsilon_r} t_{MgO}\, n_{Dy}^2$. Taking tabulated values for the MgO lattice constant $a_{MgO} = 212$ pm, relative permittivity $\epsilon_r = 9.9$, and a surface coverage of 0.01 ML of Dy corresponding to a density $n_{Dy} = 1.11 \times 10^{17}$ atoms/m^2, we find the specific electrostatic energy $\frac{\varepsilon}{(t_{MgO}\, n_{Dy})}$ = 21.5 meV per MgO layer per Dy atom. By estimating the crossover between the two configurations to occur at around 7 layers, the required electrostatic energy to overcome the configurational difference between $4f^{9}$ and $4f^{10}$ amounts to about 150 meV per Dy atom. Although this simple model neglects other MgO thickness-related effects, such as the variation of the work function,[19] the obtained value for the

configurational crossover is of the same order of magnitude of that estimated for Dy divalent compounds.[20]

SUPPLEMENTARY REFERENCES

1. Donati, F.; Rusponi, S.; Stepanow, S.; Wäckerlin, C.; Singha, A.; Persichetti, L.; Baltic, R.; Diller, K.; Patthey, F.; Fernandes, E.; Dreiser, J.; Sljivancanin, Z.; Kummer, K.; Nistor, C.; Gambardella, P.; Brune, H., Magnetic remanence in single atoms. *Science* **2016,** *352* (6283), 318-21.
2. Fernandes, E.; Donati, F.; Patthey, F.; Stavrić, S.; Šljivančanin, Ž.; Brune, H., Adsorption sites of individual metal atoms on ultrathin MgO(100) films. *Phys. Rev. B* **2017,** *96* (4), 045419.
3. Fernandes, E. Adsorption Sites of Metal Atoms on MgO Thin Films and Rotational Quantum State Spectroscopy of Physisorbed H_2. Ph.D. thesis; EPFL, Lausanne, 2017.
4. Piamonteze, C.; Flechsig, U.; Rusponi, S.; Dreiser, J.; Heidler, J.; Schmidt, M.; Wetter, R.; Calvi, M.; Schmidt, T.; Pruchova, H.; Krempasky, J.; Quitmann, C.; Brune, H.; Nolting, F., X-Treme beamline at SLS: X-ray magnetic circular and linear dichroism at high field and low temperature. *J. Synchrotron Radiat.* **2012,** *19* (Pt 5), 661-74.
5. Dreiser, J.; Westerström, R.; Piamonteze, C.; Nolting, F.; Rusponi, S.; Brune, H.; Yang, S.; Popov, A.; Dunsch, L.; Greber, T., X-ray induced demagnetization of single-molecule magnets. *Applied Physics Letters* **2014,** *105* (3), 032411.
6. Uldry, A.; Vernay, F.; Delley, B., Systematic computation of crystal-field multiplets for x-ray core spectroscopies. *Phys. Rev. B* **2012,** *85* (12), 125133.
7. Singha, A.; Willke, P.; Bilgeri, T.; Zhang, X.; Brune, H.; Donati, F.; Heinrich, A. J.; Choi, T., Engineering atomic-scale magnetic fields by dysprosium single atom magnets. *Nat. Commun.* **2021,** *12* (1), 4179.
8. Natterer, F. D.; Donati, F.; Patthey, F.; Brune, H., Thermal and Magnetic-Field Stability of Holmium Single-Atom Magnets. *Phys. Rev. Lett.* **2018,** *121* (2), 027201.
9. Donati, F., Magnetic Relaxation Mechanisms in Ho Single Atom Magnets. *J. Magn.* **2020,** *25* (4), 441-452.
10. Giannozzi, P.; Baroni, S.; Bonini, N.; Calandra, M.; Car, R.; Cavazzoni, C.; Ceresoli, D.; Chiarotti, G. L.; Cococcioni, M.; Dabo, I.; Dal Corso, A.; de Gironcoli, S.; Fabris, S.; Fratesi, G.; Gebauer, R.; Gerstmann, U.; Gougoussis, C.; Kokalj, A.; Lazzeri, M.; Martin-Samos, L.; Marzari, N.; Mauri, F.; Mazzarello, R.; Paolini, S.; Pasquarello, A.; Paulatto, L.; Sbraccia, C.; Scandolo, S.; Sclauzero, G.; Seitsonen, A. P.; Smogunov, A.; Umari, P.; Wentzcovitch, R. M., QUANTUM ESPRESSO: a modular and open-source software project for quantum simulations of materials. *J. Phys.: Condens. Matter* **2009,** *21* (39), 395502.
11. Giannozzi, P.; Andreussi, O.; Brumme, T.; Bunau, O.; Buongiorno Nardelli, M.; Calandra, M.; Car, R.; Cavazzoni, C.; Ceresoli, D.; Cococcioni, M.; Colonna, N.; Carnimeo, I.; Dal Corso, A.; de Gironcoli, S.; Delugas, P.; DiStasio, R. A.; Ferretti, A.; Floris, A.; Fratesi, G.; Fugallo, G.; Gebauer, R.; Gerstmann, U.; Giustino, F.; Gorni, T.; Jia, J.; Kawamura, M.; Ko, H. Y.; Kokalj, A.; Küçükbenli, E.; Lazzeri, M.; Marsili, M.; Marzari, N.; Mauri, F.; Nguyen, N. L.; Nguyen, H. V.; Otero-de-la-Roza, A.; Paulatto, L.; Poncé, S.; Rocca, D.; Sabatini, R.; Santra, B.; Schlipf, M.; Seitsonen, A. P.; Smogunov, A.; Timrov, I.;

Thonhauser, T.; Umari, P.; Vast, N.; Wu, X.; Baroni, S., Advanced capabilities for materials modelling with Quantum ESPRESSO. *J. Phys.: Condens. Matter* **2017,** *29* (46), 465901.
12. Dal Corso, A., Pseudopotentials periodic table: From H to Pu. *Comput. Mater. Sci.* **2014,** *95*, 337-350.
13. Prandini, G.; Marrazzo, A.; Castelli, I. E.; Mounet, N.; Marzari, N., Precision and efficiency in solid-state pseudopotential calculations. *Npj Comput. Mater.* **2018,** *4* (1), 72.
14. Blöchl, P. E., Projector augmented-wave method. *Phys. Rev. B* **1994,** *50* (24), 17953-17979.
15. Perdew, J. P.; Burke, K.; Ernzerhof, M., Generalized Gradient Approximation Made Simple. *Phys. Rev. Lett.* **1996,** *77* (18), 3865-3868.
16. Leiria Campo Jr, V.; Cococcioni, M., Extended DFT +U+Vmethod with on-site and inter-site electronic interactions. *J. Phys.: Condens. Matter* **2010,** *22* (5), 055602.
17. Topsakal, M.; Wentzcovitch, R. M., Accurate projected augmented wave (PAW) datasets for rare-earth elements (RE = La-Lu). *Comput. Mater. Sci.* **2014,** *95*, 263-270.
18. Singha, A.; Baltic, R.; Donati, F.; Wäckerlin, C.; Dreiser, J.; Persichetti, L.; Stepanow, S.; Gambardella, P.; Rusponi, S.; Brune, H., 4f-occupancy and magnetism of rare-earth atoms adsorbed on metal substrates. *Phys. Rev. B* **2017,** *96* (22), 224418.
19. Hurdax, P.; Hollerer, M.; Puschnig, P.; Lüftner, D.; Egger, L.; Ramsey, M. G.; Sterrer, M., Controlling the Charge Transfer across Thin Dielectric Interlayers. *Adv. Mater. Interfaces* **2020,** *7* (14), 2000592.
20. Fieser, M. E.; MacDonald, M. R.; Krull, B. T.; Bates, J. E.; Ziller, J. W.; Furche, F.; Evans, W. J., Structural, Spectroscopic, and Theoretical Comparison of Traditional vs Recently Discovered Ln2+ Ions in the [K(2.2.2-cryptand)][(C5H4SiMe3)3Ln] Complexes: The Variable Nature of Dy2+ and Nd2+. *J. Am. Chem. Soc.* **2015,** *137* (1), 369-382.